

AD-A167 892

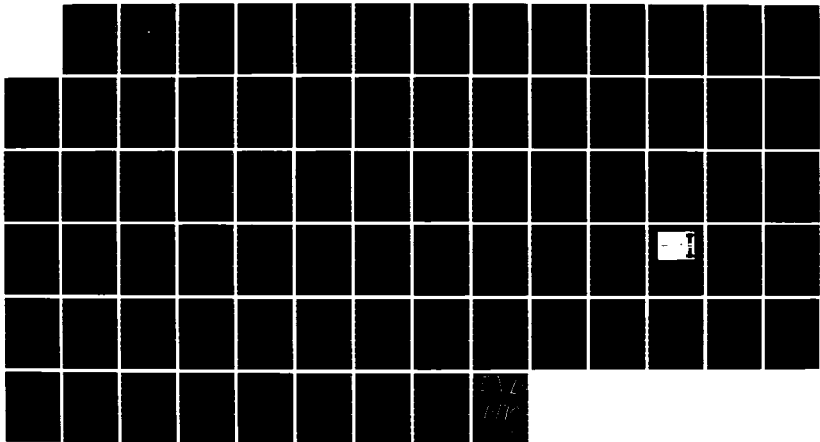
CONSTRUCTION OF A FIBER OPTIC GRADIENT HYDROPHONE USING
A NICHOLSON CONFIGURATION(U) NAVAL POSTGRADUATE SCHOOL
MONTEREY CA P A FELDMAN 27 MAR 86

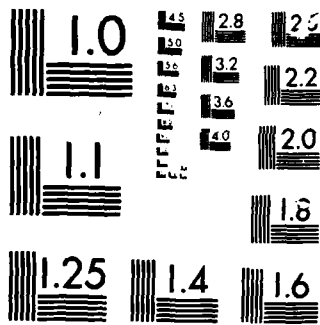
1/1

UNCLASSIFIED

F/G 20/1

NL





MICROCOPY

CHART

2

NAVAL POSTGRADUATE SCHOOL

Monterey, California

AD-A167 892



DTIC
ELECTE
MAY 29 1986
S
B

THESIS

CONSTRUCTION OF A FIBER OPTIC
GRADIENT HYDROPHONE
USING A MICHELSON CONFIGURATION

by

Peggy A. Feldmann

March 1986

Thesis Co-Advisor: S.L. Garrett
Thesis Co-Advisor: E.F. Carome

Approved for public release; distribution is unlimited

REPORT DOCUMENTATION PAGE

1a REPORT SECURITY CLASSIFICATION			1b. RESTRICTIVE MARKINGS			
2a SECURITY CLASSIFICATION AUTHORITY			3. DISTRIBUTION/AVAILABILITY OF REPORT Approved for public release; distribution is unlimited.			
2b. DECLASSIFICATION/DOWNGRADING SCHEDULE						
4 PERFORMING ORGANIZATION REPORT NUMBER(S)			5. MONITORING ORGANIZATION REPORT NUMBER(S)			
6a. NAME OF PERFORMING ORGANIZATION Naval Postgraduate School		6b. OFFICE SYMBOL (if applicable) Code 61	7a. NAME OF MONITORING ORGANIZATION Naval Postgraduate School			
6c. ADDRESS (City, State, and ZIP Code) Monterey, California 93943-5000			7b. ADDRESS (City, State, and ZIP Code) Monterey, California 93943-5000			
8a. NAME OF FUNDING/SPONSORING ORGANIZATION		8b. OFFICE SYMBOL (if applicable)	9. PROCUREMENT INSTRUMENT IDENTIFICATION NUMBER			
8c. ADDRESS (City, State, and ZIP Code)			10. SOURCE OF FUNDING NUMBERS			
			PROGRAM ELEMENT NO.	PROJECT NO.	TASK NO.	WORK UNIT ACCESSION NO.
11. TITLE (Include Security Classification) CONSTRUCTION OF A FIBER OPTIC GRADIENT HYDROPHONE USING A MICHELSON CONFIGURATION						
12. PERSONAL AUTHOR(S) Feldmann, Peggy A.						
13a. TYPE OF REPORT Master's Thesis		13b. TIME COVERED FROM _____ TO _____		14. DATE OF REPORT (Year, Month, Day) 1986 March 27	15. PAGE COUNT 76	
16. SUPPLEMENTARY NOTATION Work supported by Naval Research Laboratory (N001786WR601389).						
17. COSATI CODES			18. SUBJECT TERMS (Continue on reverse if necessary and identify by block number) fiber optics; pressure gradient hydrophone, Michelson interferometer, fiber optic sensors, dipole; unbalanced dipole.			
FIELD	GROUP	SUB-GROUP				
19. ABSTRACT (Continue on reverse if necessary and identify by block number) The fabrication and testing of a Michelson interferometric pressure gradient fiber optic hydrophone is described. The ten meter sensing fibers, wound on teflon mandrels were found to have individual coil sensitivities of .64 +/- .08 rad/Pa in the frequency range of 125 to 560 Hz. This value was a factor of twenty greater than expected based on the elastic properties of the teflon mandrels and this discrepancy is currently under investigation. The differential coil pairs exhibited the typical dipolar directionality pattern and the gradient sensitivity was consistent with the individual coil sensitivities. A discussion of gradient sensor behavior of an unbalanced dipole in both standing and traveling wave fields is included.						
20. DISTRIBUTION/AVAILABILITY OF ABSTRACT <input checked="" type="checkbox"/> UNCLASSIFIED/UNLIMITED <input type="checkbox"/> SAME AS RPT <input type="checkbox"/> DTIC USERS			21. ABSTRACT SECURITY CLASSIFICATION unclassified			
22a. NAME OF RESPONSIBLE INDIVIDUAL S.L. Garrett			22b. TELEPHONE (Include Area Code) 408-646-2540		22c. OFFICE SYMBOL Code 61Gx	

Approved for public release; distribution is unlimited.

Construction of a Fiber Optic Gradient
Hydrophone Using A Michelson Configuration

by

Peggy A. Feldmann
Lieutenant, United States Navy
B.S., United States Naval Academy, 1980

Submitted in partial fulfillment of the
requirements for the degree of

MASTER OF SCIENCE IN ENGINEERING ACOUSTICS

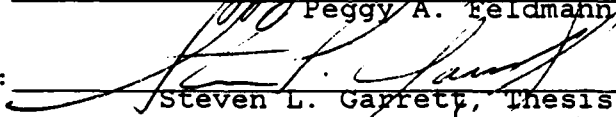
from the

NAVAL POSTGRADUATE SCHOOL
March 1986

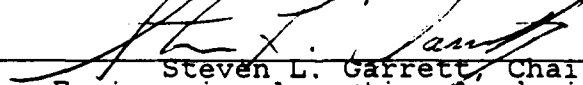
Author:

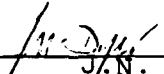

Peggy A. Feldmann

Approved by:


Steven L. Garrett, Thesis Advisor


Edward F. Carome, Co-Advisor


Steven L. Garrett, Chairman,
Engineering Acoustics Academic Committee


J.N. Dyer,
Dean of Science and Engineering

ABSTRACT

The fabrication and testing of a Michelson interferometric pressure gradient fiber optic hydrophone is described. The ten meter sensing fibers, wound on teflon mandrels, were found to have individual coil sensitivities of $.64 \pm .08$ rad/Pa in the frequency range of 125 to 560 Hz. This value was a factor of twenty greater than expected based on the elastic properties of the teflon mandrels and this discrepancy is currently under investigation. The differential coil pairs exhibited the typical dipolar directionality pattern and the gradient sensitivity was consistent with the individual coil sensitivities. A discussion of gradient sensor behavior of an unbalanced dipole in both standing and traveling wave fields is included.

Accession For	
NTIS GRA&I	<input checked="" type="checkbox"/>
DTIC TAB	<input type="checkbox"/>
Unannounced	<input type="checkbox"/>
Justification	
By	
Distribution/	
Availability Codes	
Dist	Avail and/or Special
A-1	



TABLE OF CONTENTS

I. INTRODUCTION 10

A. BACKGROUND 10

 1. Why Fiber Optics? 10

 2. What is Fiber Optics? 12

 3. Fabrication 16

 4. Transmission Links 19

 5. Future Work 21

B. FIBER OPTIC SENSORS 21

 1. Intensity Modulation 23

 2. Polarization Modulation 24

 3. Phase Modulation 25

C. PURPOSE OF THIS STUDY 27

D. FORMAT OF THE REPORT 28

II. THEORY 30

A. GRADIENT HYDROPHONE 30

 1. Traveling Wave Field 31

 2. Standing Wave Field 32

B. CALIBRATION OF GRADIENT HYDROPHONES 35

C. INTERFEROMETRY 37

 1. Electric Field Vector 37

 2. Michelson Interferometer 43

III. EXPERIMENTAL APPARATUS 45

A. MICHELSON INTERFEROMETER DESIGN AND CONSTRUCTION 45

B. INTERFEROMETER COMPONENTS 46

 1. Fiber 46

 2. Laser Source 46

 3. Polarization Controller 46

REPRODUCED AT GOVERNMENT EXPENSE

4.	3-dB Coupler	48
5.	Cable	48
6.	Teflon Mandrels	48
7.	Partially Reflecting Ends	48
8.	Power Meter	49
9.	Photodetector	49
C.	CONSTRUCTION OF MICHELSON INTERFEROMETER	50
D.	INSTRUMENTATION	52
1.	Signal Generation	52
2.	Detection	54
IV.	EXPERIMENTAL PROCEDURE AND ANALYSIS	56
A.	DIPPED HYDROPHONE	56
1.	Experimental Procedure at 255 Hz	56
2.	Experimental Procedure at 558 Hz	57
3.	Single Coil and Temperature Sensitivities	57
B.	UNDIPPED HYDROPHONE	62
V.	CONCLUSIONS	67
A.	SUMMARY OF RESULTS	67
B.	CONCLUSIONS	69
C.	RECOMMENDATIONS	70
	LIST OF REFERENCES	71
	BIBLIOGRAPHY	73
	INITIAL DISTRIBUTION LIST	74

LIST OF TABLES

I	SIZE AND WEIGHT OF CABLES	11
II	PRESENT AND FUTURE COMPONENT VALUES	21
III	SPEED OF SOUND IN 'SLOW WAVE' CALIBRATOR	52
IV	SINGLE COIL AND TEMPERATURE SENSITIVITIES OF DIPPED HYDROPHONES	61
V	SINGLE COIL AND TEMPERATURE SENSITIVITIES OF UNDIPPED HYDROPHONE	63
VI	GRADIENT SENSOR SENSITIVITIES	68

LIST OF FIGURES

1.1	Examples of Communication Systems in the Electromagnetic Spectrum	13
1.2	Reflected Ray Path at an Interface	13
1.3	Propagation Constant and Velocity of Various Modes as a Function of the V-Parameter	15
1.4	Comparison of Optical Fiber Types	17
1.5	Direct-Melt Method Using Double Crucible Arrangement	18
1.6	Schematic of a Fiber Drawing Apparatus	19
1.7	A Tapered Fiberoptic Coupler	20
1.8	Interferometric Gradient Hydrophone	28
1.9	830 nm Mach-Zehnder Interferometer	29
2.1	Geometry Used in Deriving Sensing Characteristics of Acoustic Dipole	31
2.2	Sensitivity Ratios in a Traveling Wave Field	33
2.3	Standing Wave Geometry	34
2.4	Sensitivity Ratios in a Standing Wave Field	36
2.5	Polarization Effect	39
2.6	Polarization Drift	40
2.7	Photodiode Bessel Function Response	41
2.8	Electric Field Vector Summary	43
2.9	All-Fiber Michelson Interferometer	44
3.1	Optical Fiber Michelson Interferometer	45
3.2	Laser Power vs. Source Current	47
3.3	Cleaved End of a Ten Meter Lead	49
3.4	T-bar opened to reveal coupler	51
3.5	Standing Wave Acoustic Field vs. Depth	53
3.6	Electronic Block Diagram	54
4.1	Directional Sensitivity of Dipped Hydrophone at 255 Hz	58
4.2	Directional Sensitivity of Dipped Hydrophone at 558 Hz	60

4.3	Single Coil Sensitivity Experimental Setup	61
4.4	Theoretical Sensitivity Patterns of Dipped Hydrophone	62
4.5	Theoretical and Measured Sensitivities of Undipped Hydrophone at 125 Hz	64
4.6	Theoretical and Measured Sensitivities of Undipped Hydrophone at 258 Hz	65
4.7	Theoretical and Measured Sensitivities of Undipped Hydrophone at 532 Hz	66

ACKNOWLEDGEMENTS

This thesis is dedicated to the memory of our instrument maker/machinist, Mr. Robert Moeller. Bob was truly one of the unsung heroes of American science. His contributions to this project and countless others were frequently the difference between success and failure, elegance and ambiguity. He was a gentleman, an ingenuous craftsman and a true scientist. We miss him.

I would like to thank my thesis advisors, Dr. S.L. Garrett and Dr. E.F. Carome. Their untiring enthusiasm and zeal toward science is refreshing. Thanks also to Gary Mills and Glenn MacDonald for their past work in this area, David Gardner for his assistance in the unbalanced dipole problem, and to Rick Self, who decided to "look into the subject".

Finally, a special thank you goes to my fiber winder, water swisher, typist, all around good guy and husband - Andy Brower. I do not know if I would have made it without him.

I. INTRODUCTION

A. BACKGROUND

In the past decade, optical fiber technology has advanced at a rapid pace, offering significant advantages over conventional communications techniques. An introduction into the terminology, principles, fabrication and transmission links follows.

1. Why Fiber Optics?

There are many advantages for the use of optical fibers over coaxial cables in data transmission applications. Some of these advantages are:

- * Immunity From Electromagnetic Interference. Fiber optics can be used in regions of high electric or magnetic field strength since the fibers are nonconducting. This is particularly significant when data is transmitted in the vicinity of high power a.c. (motors, power transmission lines) or r.f. (transmitters, computers, ect.) sources.
- * Lack of Sparking. When the fiber breaks, no sparking will take place, thus it can be used around flammable liquids.
- * Lack of Crosstalk. Due to the normal design of a fiber, crosstalk between lines is virtually eliminated. Problems of "ground loops" are non-existent. Separation of the lines by increased shielding (adding cost, size, and weight) is needed to eliminate crosstalk in coaxial cable.
- * No Requirement for a Radio Emission License. This is a long, drawn out process which is eliminated because the optical fiber is nonradiating.

The above advantages are most significant in applications which involve electric and electromagnetic fields. For underwater applications, the major advantages are:

- * Low Cost. The glass fibers are made from widely available silica-based materials, whereas the cost of copper, the metal constituent of a coaxial cable, fluctuates in the commodities market.

- * Wide Bandwidth. In a fiber, losses are independent of bandwidth; in a coaxial cable, bandwidth is proportional to the size of the conductors.
- * Lower Transmission Losses and Power Requirements. The number of repeaters is reduced in a long fiber link as compared to a coaxial cable. Similarly, the power requirements dictated by amplifiers which are capable of driving long coaxial cables are significantly greater than those necessary to power solid state light sources.
- * Compatibility. The small size of fiber permits direct compatibility with miniaturized electronics.
- * Light weight and small size. One fiber has the capacity to transmit as much information as hundreds of twisted pairs. The size and weight of the fiber is extremely small. This allows for easy payout and less susceptibility to hydrodynamic noise sources such as "strumming". Table I summarizes differences in size and weight [Ref. 1].

TABLE I
SIZE AND WEIGHT OF CABLES

Type of Cable	Overall Diameter (inches)	Weight in Air (lbs/naut mile)
Single-armor coaxial cable	1.25	6600
Double-armor coaxial cable	1.75	54,600
Typical optical fiber cable	0.02	2.1

There are some disadvantages to using an optical fiber system. The primary one is a lack of standards. In order to adopt standards, technological progress must slow and the community is hesitant to slow down the current rapid pace of development and innovation. At present, the only standards are for fiber dimensions. The biggest problem is with connectors. Many companies design their own connectors, leading to assembly incompatibilities. [Ref. 2: pp.2-8]

The idea of light carrying information has been around for many years. Increasing interest became obvious in 1960 with the advent of the laser. The laser, operating

in the optical frequencies near 5×10^{14} Hz, provides a coherent optical source with an information capacity theoretically exceeding that of microwave systems by a factor of 10^5 . Figure 1.1 [Ref. 3: p. 2] shows the distribution of communication systems over the electromagnetic spectrum. A number of experiments were done to show the feasibility of earth-to-space communications with an optical source. Due to the uncertainty and limitations imposed by the atmosphere, most systems were deemed economically infeasible. However, the prospect of guiding the light within an optical fiber became practical when it was proven that glass, without impurities, is a low loss one-dimensional propagation medium. [Ref. 3: pp. 1-4]

2. What is Fiber Optics?

Fiber optics is based on the principle of total internal reflection, which can be explained by Snell's Law. The index of refraction (n) in a medium is given as $n = c/v$ where c is the speed of light in a vacuum and v is the speed of light in the medium ($n = 1.00029$ for air). According to Snell's Law, it is known that $n_1 \cos \theta_1 = n_2 \cos \theta_2$ where θ_1 is the angle of incidence and θ_2 is the angle of transmission as measured with respect to the fiber axis. When a plane wave strikes an interface of a different index of refraction, n_2 , some of the energy will propagate out into n_2 while some will reflect back into the original medium, n_1 . When the ray strikes the interface at an angle greater than the critical angle of incidence, the energy will be totally reflected back into n_1 . The minimum angle θ that supports total internal reflection is the critical angle, $\sin \theta_c = n_2/n_1$. This totally reflected propagation down the medium n_1 is the basis for fiber optical transmissions. Figure 1.2 is an example of the totally reflected ray path. [Ref. 3: p. 17]

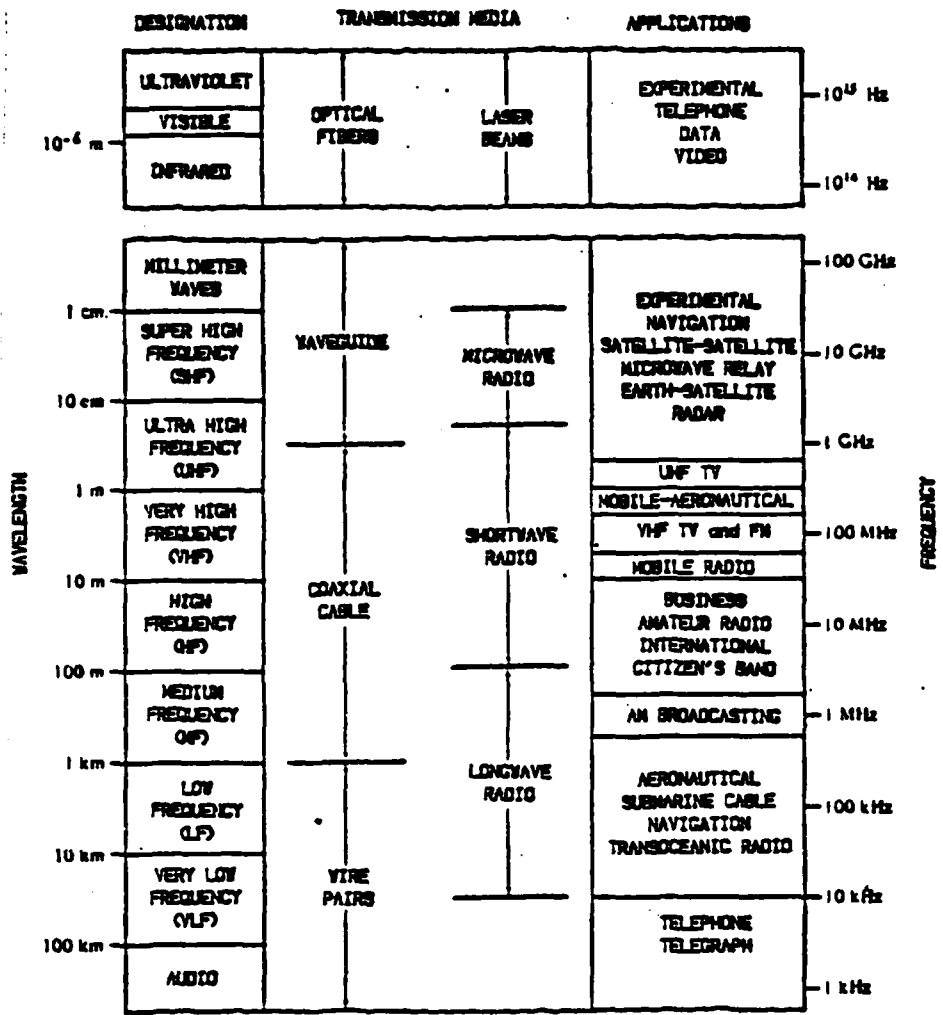


Figure 1.1 Examples of Communication Systems in the Electromagnetic Spectrum.

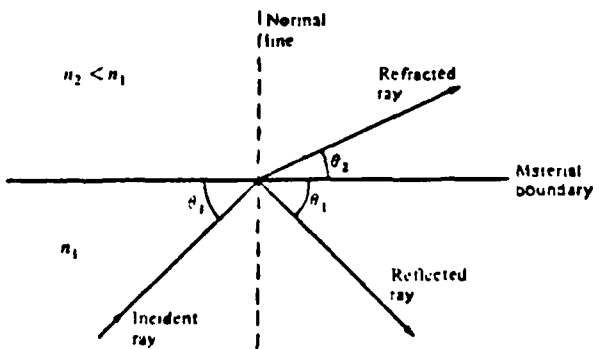


Figure 1.2 Reflected Ray Path at an Interface.

The propagating region, n_1 , is known as the core. The outer region, n_2 , is known as the cladding and is generally protected from the environment by a plastic jacketing. Typically, $n_1 = 1.48$ and $n_2 = 1.46$ but they are dependent on the manufacturer's choice of materials. The cladding-to-core index ratio is a major factor in determining the broadening of the light pulses traveling through the fiber. [Ref. 4: pp. 1-6]

An important dimensionless parameter which scales the cladding-to-core ratio is the waveguide V-parameter, also called the normalized frequency. Note that for a particular fiber, that is, given n_1 , n_2 , and a , V depends only on the frequency of the light (i.e. $1/\lambda$). The V-parameter is defined by:

$$V = 2\pi a/\lambda_0 (n_1^2 - n_2^2)^{1/2} \quad (\text{eqn 1.1})$$

where a is the core radius and λ_0 is the wavelength of the incident light in a vacuum [Ref. 5: p. 2-5]. The V-parameter establishes a relationship between the critical angle of the fiber, the number of electromagnetic modes in the fiber and the modal dispersion (the amount of dispersion caused by path differences or phase velocity differences between the modes). The number of modes in a fiber is dependent on the value of V . If V is less than 2.405, only one mode can propagate. This is the condition which exists in single mode fibers. For values of V greater than 2.405, there are numerous propagating modes which satisfy the boundary conditions imposed by the index of refraction mismatch in this cylindrical geometry; these fibers are known as multimode fibers. Figure 1.3 [Ref. 5: p. 2-5] shows the waveguide V-parameter vs. the propagation constants and the phase velocity. Ray theory can interpret how these modes travel down the fiber. The highest order

confinement process. Instead, the light refracts around the axis of the fiber tracing a sinusoidal wave path. The light travels faster in the lower index region so arrival time differences between axial and non-axial ray paths are reduced resulting in less dispersion. By doping, varying the stoichiometry by the adding of different glasses (GeO_2), the time delay can be minimized even further. Because of the lower dispersion, the graded-index fiber achieves an order of magnitude improvement over the step-index fiber in reducing the pulse broadening; the fiber can therefore handle a larger bandwidth. [Ref. 4: pp. 5-8]

Single mode fibers are designed to operate at a specified wavelength. Since there is only one mode, the fiber is not troubled by the mode-to-mode velocity dependence of the multimode fiber. However, all sources of light in a medium have some spread of frequencies or wavelength (i.e. spectral width) and this implies the longer wavelengths will arrive sooner than the short wavelengths due to increased velocities. This difference is caused by two effects known as waveguide and material dispersion. Silica's material dispersion has a minimum value at a wavelength of 1.27 μmeter . At this wavelength a third type of dispersion, waveguide dispersion, becomes important. The positive waveguide dispersion cancels the negative material dispersion at 1.33 μmeter for silica. Therefore, a single mode fiber has a maximum bandwidth capacity at 1.33 μmeter . Figure 1.4 [Ref. 6: pp. 43,49] compares the three types of optical fibers.

3. Fabrication

Glass does not have an actual melting point but rather a "melting temperature". In this temperature range, glass becomes a viscous liquid and can be drawn to different lengths and widths depending on the materials used and the amount of tension that is applied to pull the glass apart.

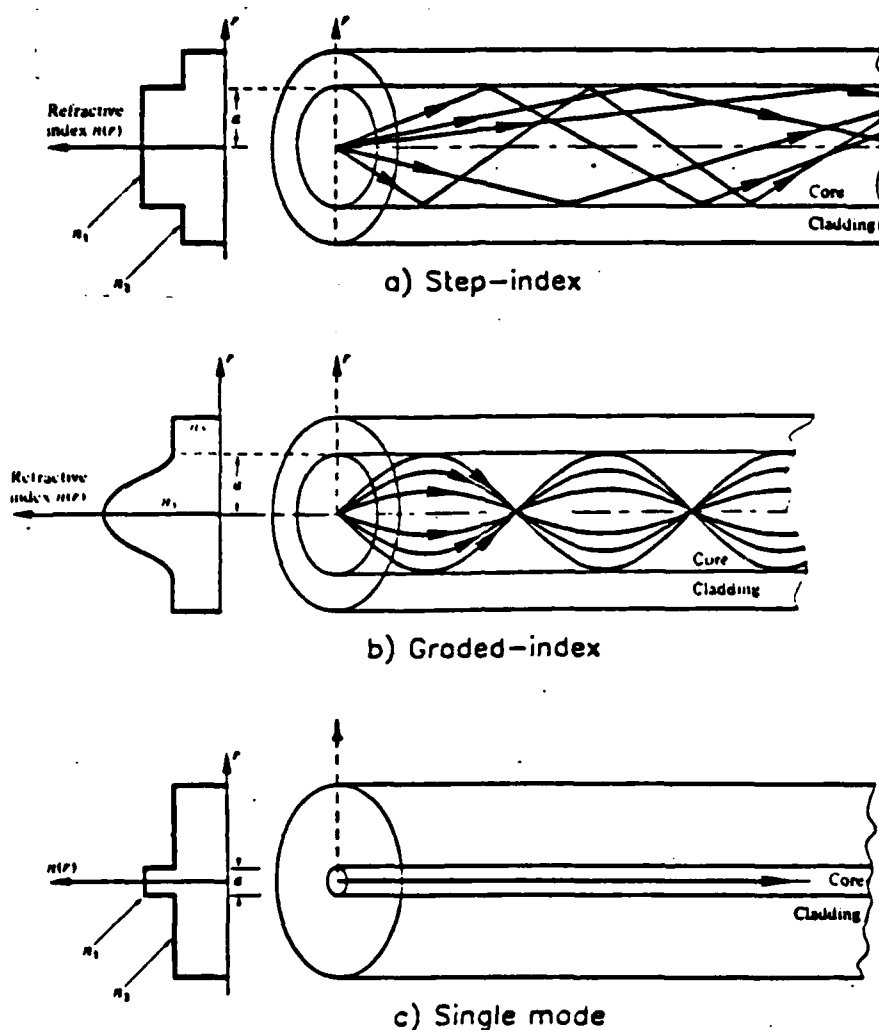


Figure 1.4 Comparison of Optical Fiber Types.

There are two basic techniques for fabricating fiber optical cables. The direct melt method, Figure 1.5 [Ref. 3: p. 275], allows multicomponent glasses like sodium biosilicate to be manufactured at low temperatures, $600^\circ - 800^\circ$ C. Purified rods of the appropriate composition are made separately and fed into two concentric crucibles, one for the core and one for the cladding. The core and cladding are drawn in a continuous production process. Additional feed rods can be added allowing for extremely long (25 km) fiber

cables to be produced. The major problem with this technique is keeping the area around the crucibles clean so as not to introduce impurities into the fiber. [Ref. 3: pp. 273-288]

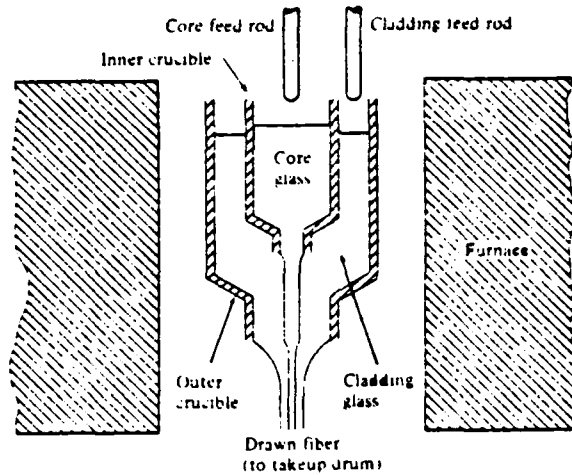


Figure 1.5 Direct-Melt Method Using Double Crucible Arrangement.

The fibers produced in the direct-melt method are not high quality fibers. In order to manufacture high performance silica fibers, temperatures of 2000° C are needed. A rod, known as a preform, is made which is an exact scaled version of the fiber to be drawn. The preform is several millimeters in diameter and may be one meter or longer in length, containing the core and the cladding. There are several different ways to make the rod. The preform is clamped to the drawing apparatus, Figure 1.6 [Ref. 3: p. 282], and an automated process draws the fiber. Manufacturers allow only a plus or minus two percent change in the diameter of the fiber, and great care is taken to assure that the fiber is as uniform as possible. Multi-mode fiber drawn from this process usually have a 125 μm or 200 μm cladding outer diameter. For single mode fibers, the most common fiber cladding outer diameter is 125 μm . In

this work, however, special fiber with a cladding outer diameter of 75 μm was used. [Ref. 2]

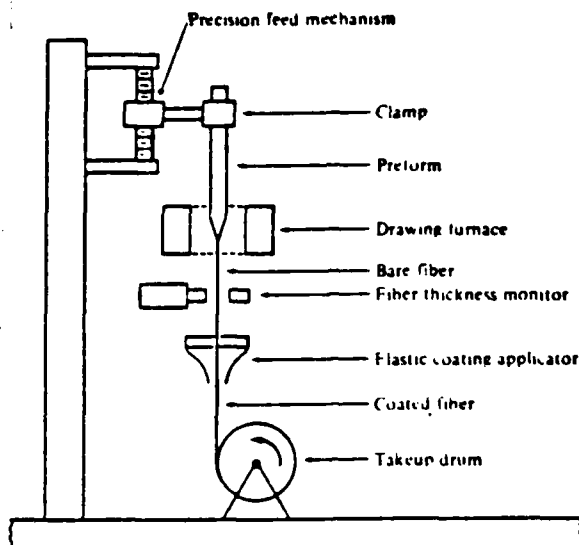


Figure 1.6 Schematic of a Fiber Drawing Apparatus.

4. Transmission Links

The standard fiber cable is usually only several kilometers long, therefore connectors or splices must be used to extend the length of the cable. Connectors allow two parts of a cable to be joined and taken apart; splices are permanent joints. Many different factors can cause losses to occur while attempting to place the ends of two very small fibers together. Some of the losses are due to the properties of the fibers and some are due to external factors. Properties within the fiber that cause losses are modal, numerical aperture, radius, index of refraction, and manufacturing dissimilarities. External factors which degrade the system are axial, longitudinal, and angular misalignment. [Ref. 2: pp. 187-194]

Care must be taken to ensure the exposed fiber is not damaged during linkage. Special devices have been made which allow the fibers to be put end to end with the least

amount of power loss. The technique of splicing has been refined to the point of 0.02 dB loss per splice. [Ref. 5: p. 3-4]

A coupler allows the beam emitted from the laser to be split into two or more fibers as indicated in Figure 1.7. While there are several coupling techniques available, the method explained below was used to manufacture the couplers used in this experiment.

Two fibers have the jacketing removed and are twisted together, a portion of the cladding is then removed by etching and the fibers are heated. Since glass stretches when heated, the fibers are pulled so that the cores are very close. The optical energy that was confined to the core tends to spread into the cladding region where the fiber has been stretched. The result is a stronger overlap and thus a high coupling ratio. A laser is put at one end of the fibers and two photodetectors at the other ends. When the light in both detectors is 50 percent (3-dB down), the joint is fixed or ruggedized. Figure 1.7 [Ref. 5: pp. 3-4], is an example of a 2x2 coupler. The light does not travel into length 2 due to the directionality of the coupler.

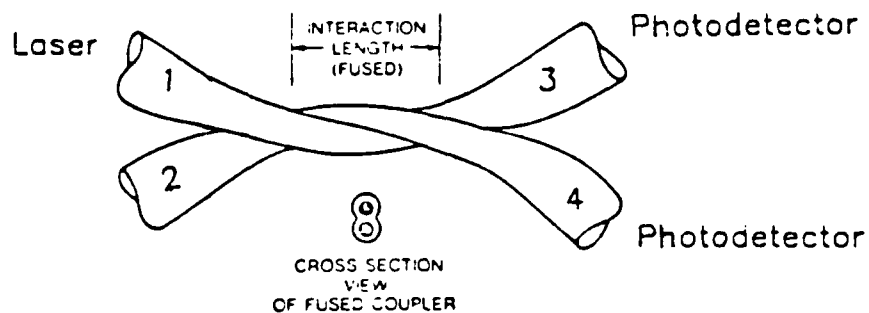


Figure 1.7 A Tapered Fiberoptic Coupler.

5. Future Work

In 1978, it was discovered that super long wavelengths in the 2 to 5 μ meter range have extremely low transmission losses [Ref. 3: pp. 273-288]. Fluorozirconates used as a medium for this region are expected to have a 0.001 to 0.01 dB/km loss. Lead selenium telluride detectors will be used in this near- to mid-infrared region. Problems that must be overcome in order to work in this region are drawing techniques and cabling. Only short fiber lengths have been produced because present drawing techniques are not applicable for the crystalline structure of the fluorides. Table II [Ref. 7], shows the present day and expected systems.

TABLE II
PRESENT AND FUTURE COMPONENT VALUES

	Conventional	Long Wavelength		Super Long Wavelength
Wavelength	0.8 to 0.9 μ m.	1.3 μ m.	1.5 μ m.	2-10 μ m.
Source	GaAlAs	InGaAsP	InGaAsP	PbSnTe
Detector	Si	Ge, InGaAsP	InGaAsP	HgCdTe
Fiber Loss	3-5 db./km.	0.5-1.5 db./km.	0.2-0.5 db./km.	Projected .001-.01 db./km.
Distance (LED)	~3 km.	~10 km.	> 10 km.	> 100 km.
(ILD)	~10 km.	~30 km.	~100 km.	> 1,000 km.
Status	Mature	Emerging	Laboratory	Research

B. FIBER OPTIC SENSORS¹

The development of low-loss optical fibers, near-infrared semiconductor lasers, and the refinement of semiconductor diodes as photodetectors has lead to the exploitation of optical fibers as transduction elements for physical measurements. Fiber optic sensors have been designed to measure pressure, temperature, electric current,

¹This section from [Ref. 8: pp. 7-11] and [Refs. 9,10].

acceleration, force, magnetic or electric field intensities, trace vapor presence, fluid level, angular and linear position and velocity. Over sixty different types of sensors using fiber optics for transduction have been designed. Some advantages of fiber over conventional transduction materials are: low cost, light weight, increased sensitivity, reduced complexity, geometric versatility since fiber sensors can be configured into arbitrary shapes and the ability to operate without d.c. electrical power for preamplifiers or signal conditioning amplifiers. This allows the design of an all fiber system to exploit compatibility with the optical data transmission.

A transducer is defined as a device that converts input energy into output energy of another form. A hydrophone is a particular type of transducer that is characterized by its ability to transform input acoustic energy in water to an energy form suitable for transmission and/or information processing. The most common transduction mechanism of current hydrophone technology is piezoelectricity, defined as the production of electric charge separation by application of mechanical stress to a solid. Fiber optic acoustic sensors (FOAS) rely on quite different mechanisms of energy conversion, a characteristic that converts the actions of an external agency into output signals. The first stage is preliminary conversion, where the quantity to be measured alters the optical parameters of the transmission medium. Although pressure variations represent the quantity of interest for hydrophones, fiber optic sensors are capable of measuring a wide variety of external perturbations.

The second stage of a typical FOAS is the optical modulation system. This stage transforms the original modulation of amplitude, phase, polarization, or frequency into modulation of a more desirable parameter of the transmitted optical wave. Such optical modulation systems employ a number of techniques, including the following:

- * Amplitude (intensity) Modulation is achieved by frustrated total internal reflection or variable transmissibility;
- * Polarization Modulation is achieved by rotating the plane of polarization and by taking advantage of the birefringence;
- * Phase Modulation is achieved by changing the optical length of the detection fiber.

1. Intensity Modulation

Fiber optic sensors using amplitude modulation (AM) of the sensing beam offer greater simplicity of design than phase modulation (PM) schemes because there is no need for transmodulation prior to signal processing. Furthermore, most AM systems can function with incoherent optical sources. The disadvantage of such sensors vis-a-vis phase or polarization modulated versions is lower sensitivity and in some cases a sensitivity which is dependent on optical source strength. For some systems in current use, the modulated optical intensity is only a small fraction of the total light throughput making the systems particularly sensitive to drift.

Acoustic oscillations acting on a sensing fiber varies losses in the light wave intensity with respect to those expected under static conditions. In general, optical wave amplitude can be modulated by:

- * altering waveguide cross sectional area;
- * frustrating total internal reflection;
- * controlled coupling of waveguides;
- * varying the absorption coefficient;
- * light generation.

Variations of the first two of these methods account for the majority of successful acoustic detectors to date. The controlled coupling techniques suffer from technological complexity and the mechanical difficulties encountered in

coupling thin-film (planar) and fiber (cylindrical) waveguides. Variable absorption techniques offer design simplicity for temperature, radiation and electric field detection, but the difficulty in identifying materials that respond to acoustic perturbations with suitable modulation of absorption coefficients precludes such designs from effective employment as FOAS. Finally, the principles of operation of light-generation sensors are incompatible with detection of acoustic excitation. Sonoluminescence is only produced in sound fields sufficient to produce cavitation [Ref. 11].

The simplicity and ready availability of constituent components make AM sensors excellent candidates for low-cost mass production. For hydrophone applications, however, the reduced sensitivity and dependence on light source power stability pose significant obstacles. Light emitting diodes, for example, show a strong temperature dependence which requires compensation for acceptable sensor operation. The resulting feedback networks provide adequate stabilization but negate the benefits of simplicity promised by the modulation technique.

2. Polarization Modulation

An optical wave propagating along a single-mode fiber is actually a superposition of two degenerate modes of opposite polarization rotation. The wave's polarization state is unchanged if the medium is isotropic, perfectly circular in cross section, and not subjected to mechanical stresses. Ideally the two modes do not interact and remain in quadrature but inhomogeneities in real fibers induce beating and energy transfer between modes. Consequently, a real optical fiber (particularly in the presence of stresses that induce anisotropic changes in refractive indices) exhibits birefringence properties that can be used to modulate sensing beam polarization. There is another method of

polarization modulation which involves rotating the ellipsoid of polarization but is used exclusively for electric and magnetic field measurement.

A major difference between polarization devices and phase or amplitude devices is the presence of polarizers and analyzers. The effect of these components on reducing photodetector input power often limits the sensor's dynamic range. Furthermore, organic film polarizers restrict ambient temperatures to an upper limit of about 50° C. Nonetheless, these FOAS offer reasonable sensitivity, simplicity of construction, reliability and temperature stability.

3. Phase Modulation

The most sensitive FOAS to date are those that employ phase modulation of the optical wave that transverses the medium of interest (in this case, the optical fiber). When the external agency interacts with the waveguide, the lightwave's instantaneous phase angle varies in proportion to the disturbance. Modern interferometry techniques allow detection of phase shifts as small as 1 μ radian; this equates to extremely small strains on the order of 10^{-12} in one meter of fiber when using near infrared wavelengths (\sim 1 micron).

When an optical fiber is exposed to a mechanical stress, such as an acoustical field, its physical characteristics change in response. While minor changes can occur in transverse geometric dimensions and indices of refraction (photoelastic effect), the most significant variable is waveguide physical length (Poisson effect). Since any of a number of environmental factors (temperature, acceleration, electric or magnetic fields, static pressure, etc.) can each impart mechanical stresses, sensor construction must minimize or compensate for the undesired response to such factors. The variable component of phase, $\Delta\psi$, is generally

given by Equation 1.2, where k is the wave propagation constant $= 2\pi/\lambda$, L is the waveguide length, a is the core radius, and n is the core's refractive index. The phase shift, $\Delta\psi$, is dominated by changes in fiber length for transverse stresses.

$$\Delta\psi = k\Delta L + L(\Delta n \partial k/\partial n + \Delta a \partial n/\partial a) \quad (\text{eqn 1.2})$$

The sensing element configuration usually consists of a length of fiber wrapped tightly around a compliant mandrel (i.e. Teflon).² Pressure may be applied to either the outside of the assembly or, in the case of hollow cylinders, to the inside. The action of this applied pressure is to expand or shrink the mandrel radius and, in so doing, change fiber length. Mandrel use can increase sensitivity by as much as 15 dB or more.

Phase modulation (PM) fiber sensors typically fall into one of the following categories:

- * Mach-Zender interferometers;
- * Michelson interferometers;
- * Fabry-Perot interferometers;
- * Intermode interferometers;
- * Sagnac interferometers.

Of these, the first two categories show the most promise for hydrophone applications. The Fabry-Perot design is an excellent tool for precision length measurements but is extremely sensitive to small deviations from quadrature alignment, a factor that limits its usefulness in situations where substantial static drift is expected. Intermode devices compensate for static phase shift quite effectively but suffer from poor sensitivity relative to the single mode

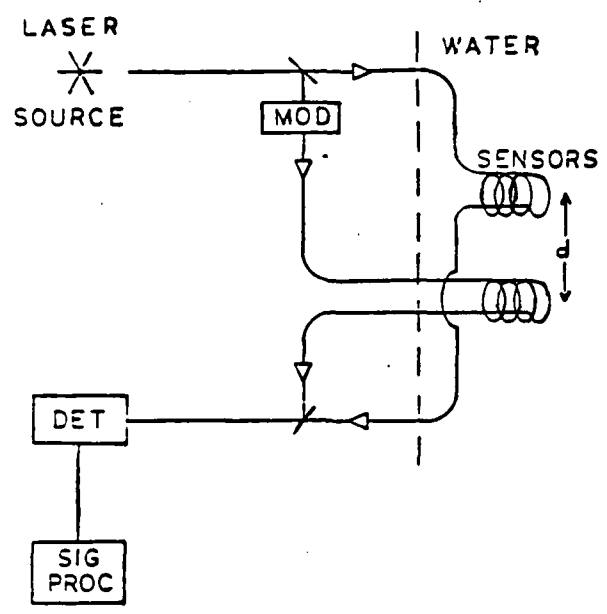
²Teflon is a registered trademark.

interferometers (6-18 dB). Finally, Sagnac interferometers are designed for angular velocity and acceleration measurement and have no known application as acoustic sensors.

Photodetector systems constitute the final stage of the energy conversion process. Although the parameter finally measured is virtually always optical intensity, many photodetector systems are available that decode other modulation schemes. The resulting sensor output signal is suitable for further processing and/or electrical transmission. The inherent compatibility of fiber optic sensors and fiber communication channels encourages direct transmission of the modulated optical wave in many applications. The ability of fiber optic sensors to measure various physical effects, coupled with the wide variety of modulation and photodetection schemes available, allow for numerous combinations of methods and components within a sensor. Consequently, the literature commonly groups sensors according to the optical modulation system because it usually determines the preliminary conversion and photodetector systems.

C. PURPOSE OF THIS STUDY

Research at the Naval Postgraduate School in the area of fiber optic acoustic sensors [Refs. 12,13,14] utilizes acoustically induced phase modulation for transduction. Figure 1.8 [Ref. 14: p. 16], illustrates the laser beam being split into two arms of an interferometer as is typical of our fiber optic pressure gradient hydrophones. Both sensing coils are exposed to the acoustic field. The two beams are recombined and allowed to interfere before reaching the photodetector. The two-arm design and high sensitivity have suggested that the interferometric design be used as a gradient-type hydrophone. A fiber optic gradient hydrophone has both arms exposed to the acoustic field. The spatial variation of the pressure field at the two coil locations provides the desired signal.



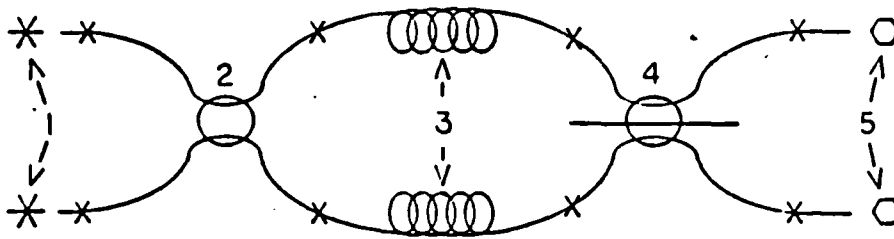
- BOTH SENSOR AND REFERENCE COIL INSONIFIED
- DETECTS SPATIAL VARIATION IN EXCITATION FIELD

Figure 1.8 Interferometric Gradient Hydrophone.

Mills and MacDonald used a Mach-Zender interferometer configuration. Figure 1.9 [Ref. 14: p. 16], illustrates that a number of splices (between 6 and 10 depending on the system) and two couplers were required in the fabrication of their hydrophones. The splices account for the majority of losses in the system. The aim of this project was to simplify the design by constructing and evaluating a Michelson interferometer which uses only three splices and one coupler. The Michelson configuration has the additional advantages of being twice as sensitive for the same sensor fiber length and more stable.

D. FORMAT OF THE REPORT

Chapter II presents the theoretical basis of conventional gradient hydrophones, distinguishing between balanced and unbalanced pairs. It also discusses the calibration of



- | | |
|----------------------|----------------------|
| 1. LASER | 4. 3 X 3 3dB COUPLER |
| 2. 2 X 2 3dB COUPLER | 5. PHOTODETECTOR |
| 3. SENSOR | X-INDICATES SPLICE |

Figure 1.9 830 nm Mach-Zehnder Interferometer.

gradient hydrophones, the behavior of interferometric fiber optic sensors and the Michelson interferometer in particular. Chapter III describes the design of the Michelson interferometer and the components used to build two systems analyzed here. A section on the construction of the systems and the instrumentation used to generate and detect signals from the interferometer are also presented in Chapter III. Experimental procedures, analysis of the data and evaluation of the results is presented in Chapter IV. Chapter V contains concluding remarks and recommendations for future work.

II. THEORY

A. GRADIENT HYDROPHONE

In many underwater scenarios it is useful to be able to determine the direction from which an acoustic signal originated. The simplest design which provides some directivity is the dipolar pressure gradient hydrophone.

A dipolar pressure gradient hydrophone is constructed so that the hydrophone's output is proportional to the difference between the pressures at two different locations in the acoustic sound field. Therefore, the output is proportional to the pressure gradient in the sound field. The main characteristic and advantage of a pressure gradient hydrophone is the directivity pattern obtained from a device of such compact dimensions. As will be shown below, balanced pressure gradient hydrophones have dipole, or "figure-eight", directivity patterns, hence they are bidirectional. Assuming the size of the hydrophone is small compared to the acoustic wavelength, λ , the dipole response when oriented at any angle θ relative to an incoming plane pressure wave is proportional to $\cos\theta$. Both for simplicity and since they resemble the fiber optic systems under study, pressure gradient hydrophones formed by combining two small, closely spaced, individual, pressure hydrophones will be discussed. The performance of this hydrophone pair (or doublet) can be calculated, and the behavior thus derived applies to pressure gradient hydrophones of more complicated construction as long as the assumptions of compactness made in the derivation are not violated. [Ref. 13: pp. 17-19]

Consider two small pressure sensors in an acoustic wave field. Two cases will be analyzed, the pressure gradient

hydrophone response in a traveling wave field and in a standing wave field.

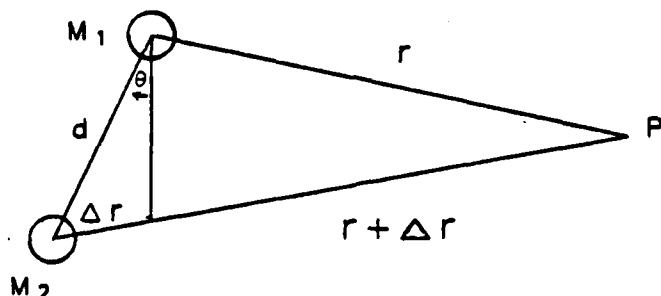


Figure 2.1 Geometry Used in Deriving Sensing Characteristics of Acoustic Dipole.

1. Traveling Wave Field

As depicted in Figure 2.1, in a traveling wave field, the instantaneous output signal from two hydrophones at points spaced a distance, d , apart (where d is much less than r , the range to the given point source) is given by equations 2.1 and 2.2:

$$e_1 = P_0 M_1 e^{j(\omega t - kr)} \quad (\text{eqn 2.1})$$

$$e_2 = P_0 M_2 e^{j(\omega t - k(r + \Delta r))} \quad (\text{eqn 2.2})$$

M_1 and M_2 are the individual sensor sensitivities. For conventional piezoelectric hydrophones the units of M are volts/Pa whereas for a fiber sensor, M has the units of radians (of phase shift)/Pa. ω is the angular frequency, t is time, k is the acoustical propagation wave number equal to $2\pi/\lambda$ where λ is the acoustic wavelength, r is the range to the source and Δr is $d \sin \theta$. The instantaneous difference in the two hydrophone signals, Δe , is defined by equation 2.3.

$$\Delta e(\theta, t) = P_0(M_1 - M_2 e^{jk\Delta r}) e^{j(\omega t - kr)} \quad (\text{eqn 2.3})$$

From the geometry in Figure 2.1, the amplitude of this variation can be written in the form of equation 2.4:

$$\Delta e(\theta) = P_0(M_1 - M_2 e^{jk d \sin \theta}) \quad (\text{eqn 2.4})$$

The magnitude of $\Delta e(\theta)$ becomes:

$$|\Delta e(\theta)| = P_0(M_1^2 + M_2^2 - 2M_1 M_2 \cos(kd \sin \theta))^{1/2} \quad (\text{eqn 2.5})$$

For a given sound field, consider the variation of the difference signal magnitude, $\Delta e(\theta)$, as the sensor pair is rotated in the field, i.e. as θ is varied. If the hydrophone is balanced, $M_1 = M_2$, the "figure-eight" pattern shown in Figure 2.2a is produced for wavelengths large compared to the sensor separation. Note that the sensitivity in Figure 2.2a is a linearly increasing function of frequency.

If the hydrophone is unbalanced, $M_1 \neq M_2$, minima and maxima will still occur but the two sensors will not exactly cancel each other. If one sensor sensitivity is much greater than the other, the sensor with the greater sensitivity will completely overpower the other sensor and the output becomes omni directional. Figures 2.2b-d provide three different sensitivity ratios in a traveling wave field with $k = 2\pi f/c$ where $f = 255$ Hz and $c = 1500$ m/sec, and $d = 0.1$ m.

2. Standing Wave Field

The instantaneous acoustic pressure $P(L, t)$ at a point along a standing wave in a tube of water is given by equation 2.6, where the depth, L , has been chosen to be zero at the air-water interface and k is the propagation wave number equal to $2\pi/\lambda$. Figure 2.3 depicts two sensors with a separation distance, d , placed in the tube so that the axis of the hydrophone is at L .

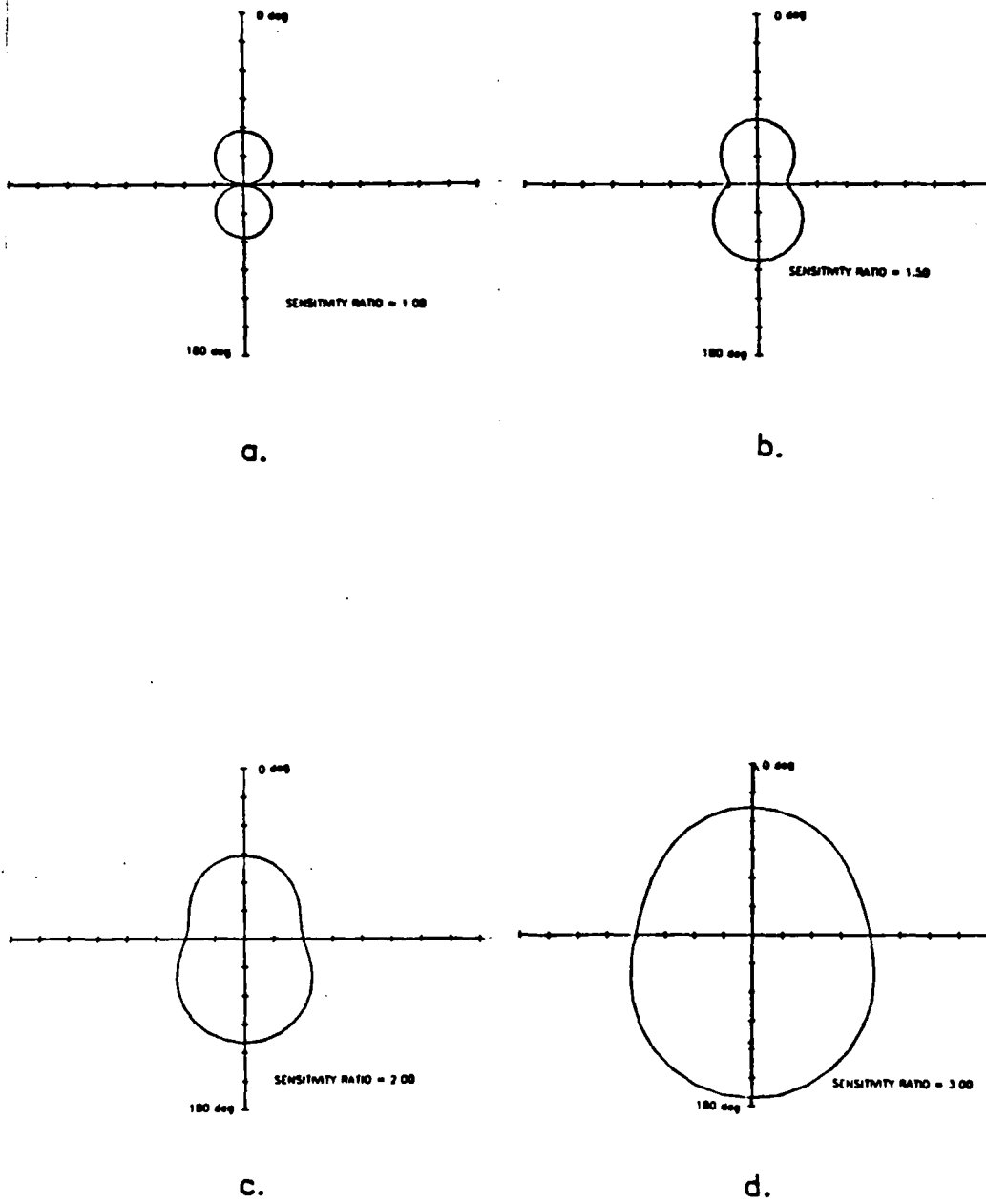


Figure 2.2 Sensitivity Ratios in a Traveling Wave Field.

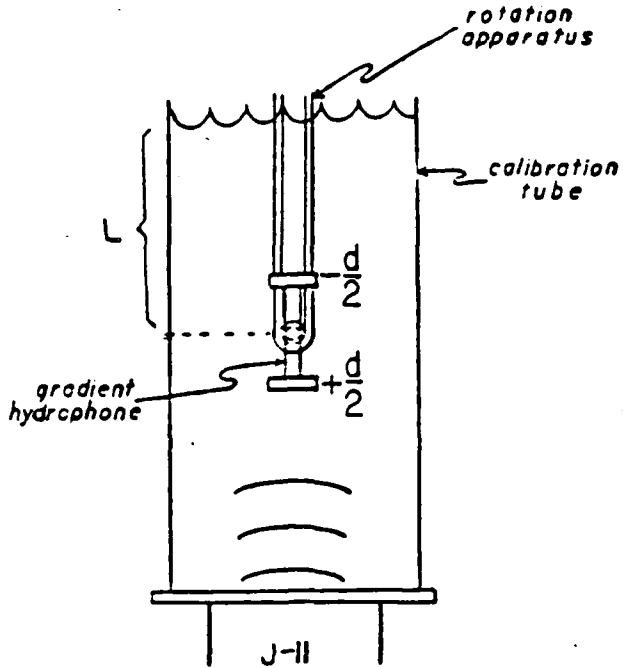


Figure 2.3 Standing Wave Geometry.

$$P(L, t) = P_0 \sin(kL) e^{j\omega t} \quad (\text{eqn 2.6})$$

The magnitude of the difference of the output signal between the two sensors, $\Delta e(L)$, is then given by equation 2.7.

$$\Delta e(L) = P_0 (M_1 \sin k(L-d/2) - M_2 \sin k(L+d/2)) \quad (\text{eqn 2.7})$$

where M_1 and M_2 are the individual sensor sensitivities. If the hydrophone is then rotated about its axis, Δe becomes Equation 2.8.

$$\Delta e(\theta) = P_0 (M_1 \sin(k(L-d\cos\theta/2)) - M_2 \sin(k(L+d\cos\theta/2))) \quad (\text{eqn 2.8})$$

As expected, a "figure-eight" pattern will be produced if the hydrophone is balanced. However, if the hydrophone is not balanced, the patterns that occur are different from those that occur in the traveling wave case. In fact, at a

specific sensitivity ratio and wave number a cardioid pattern can be generated. Figures 2.4b-d provide three different sensitivity ratios as indicated for a wave number of 5.54 m^{-1} .

B. CALIBRATION OF GRADIENT HYDROPHONES³

Pressure gradient hydrophones are usually calibrated in terms of pressure (pressure gradient is rarely used as a reference) and, therefore, the sensitivity of pressure gradient hydrophones is usually given in terms of volts/micropascals ($\text{V}/\mu\text{Pa}$), specified at a particular frequency.

The standard procedure for pressure gradient hydrophone calibration is by direct comparison with a standard pressure hydrophone and is only valid if essentially plane waves impinge on both hydrophones. Waves in a free field are never perfectly plane. If a spherically diverging wave from a point source is used, a correction factor, $10\log(1+\lambda^2/(2\pi r)^2)$, where r , the distance from the source, must be subtracted from the measured sensitivity [Ref. 15]. This correction factor decreases as r increases.

Because of the difficulties in obtaining free-field conditions, particularly at low frequencies, a standing-wave tube was employed for the laboratory investigations described in this report. Since a water-air boundary is a near zero impedance boundary, essentially complete reflection will take place at the top of the tube. A standing-wave field then can be established and equations 2.9, 2.10 and 2.11 hold in the ideal case.

If the pressure is measured at a point a distance L from the water-air surface, equations 2.9 and 2.10 can be used to compute the pressure at any other point. As stated earlier, the hydrophones are assumed to have a negligible effect on

³This section from Mills [Ref. 13: pp. 27-29].

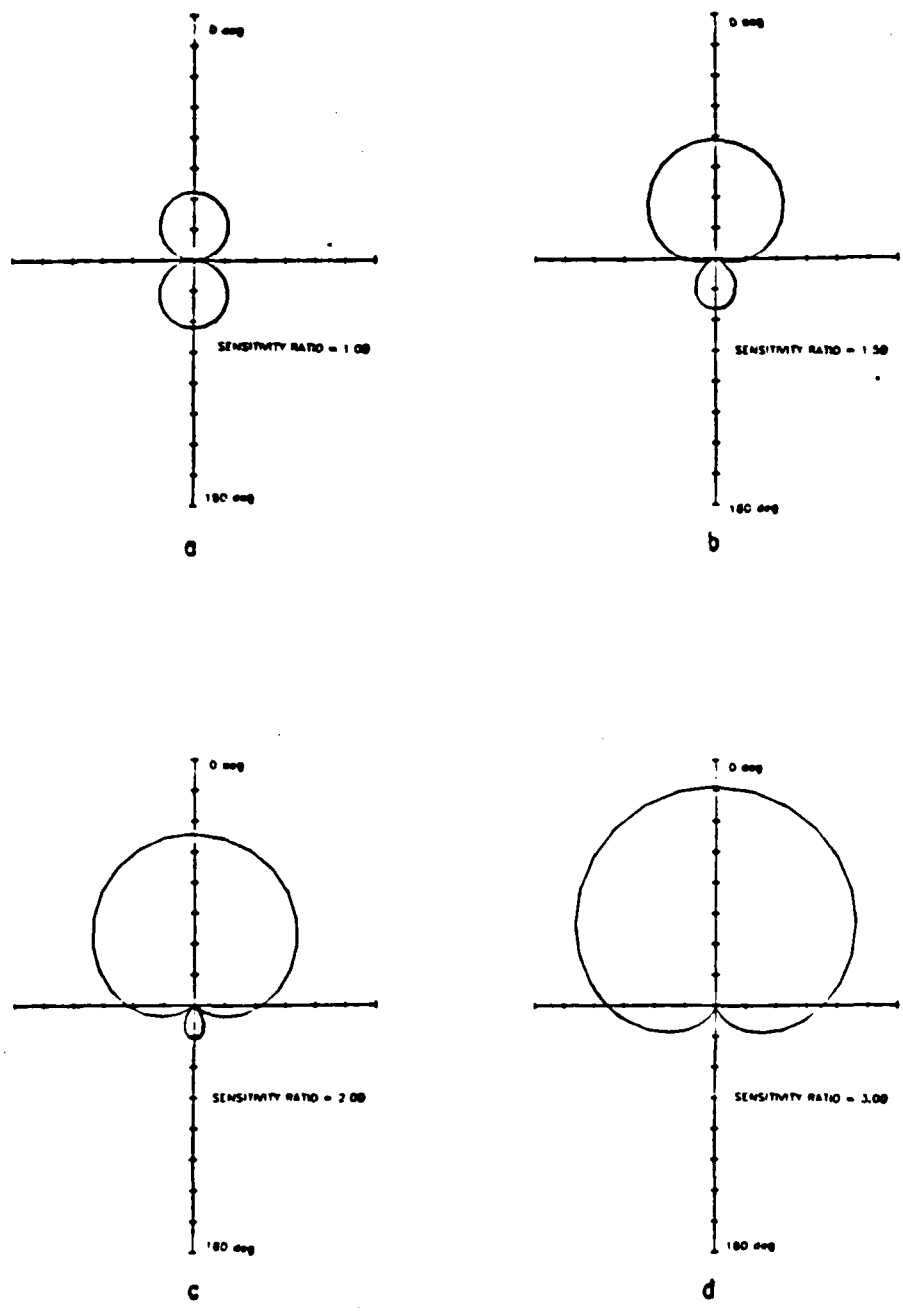


Figure 2.4 Sensitivity Ratios in a Standing Wave Field.

the standing wave pattern. If the tube is operated below cutoff for non-axial modes, then the pressure variations normal to the tube axis can be neglected.

$$p = p_0 \sin(kL) \quad (\text{eqn 2.9})$$

$$u = (p_0/\rho c) \cos(kL) \quad (\text{eqn 2.10})$$

$$p/u = \rho c \tan(kL) \quad (\text{eqn 2.11})$$

A more detailed explanation of sensitivity can be found in Bobber [Ref. 15]. In this experiment, sensitivities of single coil fiber optic acoustic hydrophones are defined in terms of radians/Pa. Sensitivities of gradient (dual coil) hydrophones are defined in terms of optical phase shifts induced by acoustic pressures and are expressed in radians/Pa at a specified frequency. The procedures used to obtain fiber optic hydrophone sensitivities (single and dual coil designs) are discussed in Chapter IV. A thorough presentation on fiber optic acoustic sensitivity is given by Davis, Carome, et al., [Ref. 5: pp. 4-1-13].

C. INTERFEROMETRY

As stated in Chapter 1 (B,3), the lightwave in the fiber may experience a phase shift due to a number of factors. Changes in fiber length and refractive index dominate as shown in equation 1.2.

1. Electric Field Vector

As stated in Self [Ref. 8: pp. 11-12], the optical wave's electric field vector will experience time harmonic variation under the influence of an acoustic signal as given by equation 2.12.

REPRODUCED AT GOVERNMENT EXPENSE

$$E_s(t) = E_0 e^{j(\omega_0 t + A \sin(\omega_a t))} \quad (\text{eqn 2.12})$$

where A is the amplitude of the acoustically induced phase shift, ω_0 is the light source angular frequency (assuming a coherent laser source), and ω_a is the acoustic field angular frequency. Interferometry is typically used to detect this phase modulation because photodetector response to such high frequencies is inadequate. This technique converts high frequency phase modulation into a lower frequency intensity modulation, thereby facilitating use of the photodetector for detection. The principle of operation involves mixing the two coherent sensing beams to form a time-varying interference pattern. Homodyne interferometers use an optical frequency that is identical in both arms, whereas heterodyne versions mix two or more optical frequencies. If homodyne techniques are considered for clarity of discussion, the electric field vector in one arm of the interferometer can be chosen as the reference electric field vector present at the mixer (coupler) given by equation 2.13, where ψ_0 represents a static phase difference attributed to non-acoustic causes such as optical path length differences, thermal expansion, etc.

$$E_r(t) = E_r e^{j(\omega_0 t + \psi_0)} \quad (\text{eqn 2.13})$$

The electric field vector incident on the photodetector, E_p , is the sum of the fields in the two beams as shown in Equation 2.14.

$$E_p(t) = E_s(t) + E_r(t) \quad (\text{eqn 2.14})$$

Initially in what follows, it is assumed that the two beams have the same direction of polarization. Due to twists and birefringence in the fiber, the $E_s(t)$ electric

field vector may not be co-linearly polarized relative to that of $E_r(t)$, and only $E_s \cos\theta$ can interfere optically with the reference arm electric field vector, $E_r(t)$. Here θ is the angle between the two directions of polarization. The ratio $E_s \cos\theta / E_r$ then determines the modulation depth or fringe visibility. Figure 2.5 illustrates this polarization effect and Figure 2.6 presents actual data showing polarization drift.

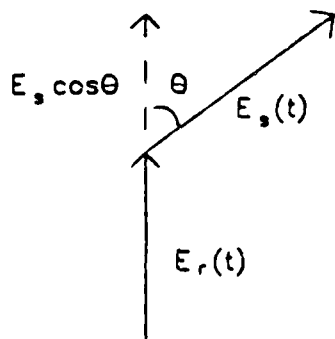


Figure 2.5 Polarization Effect.

Photodetectors produce an output current, $i(t)$, that is proportional to the incident light wave intensity, $I(t)$. Electromagnetic wave intensity is, in turn, proportional to the magnitude of the squared electric field vector. Following Carome and Satyshur [Ref. 16] and ignoring all terms of optical frequency, we obtain the following expansion for $I(t)$:

$$\begin{aligned}
 I(t) &\propto E_s^2 + E_r^2 + 2\mathbf{E}_s \cdot \mathbf{E}_r \cos\psi_0 J_0(kx) \\
 &+ 2\mathbf{E}_s \cdot \mathbf{E}_r \cos\psi_0 \sum_{n=1}^{\infty} J_{2n}(kx) \cos(2n(\omega_a t)) \quad (\text{eqn 2.15}) \\
 &+ 2\mathbf{E}_s \cdot \mathbf{E}_r \sin\psi_0 \sum_{m=0}^{\infty} J_{2m+1}(kx) \sin((2m+1)\omega_a t)
 \end{aligned}$$

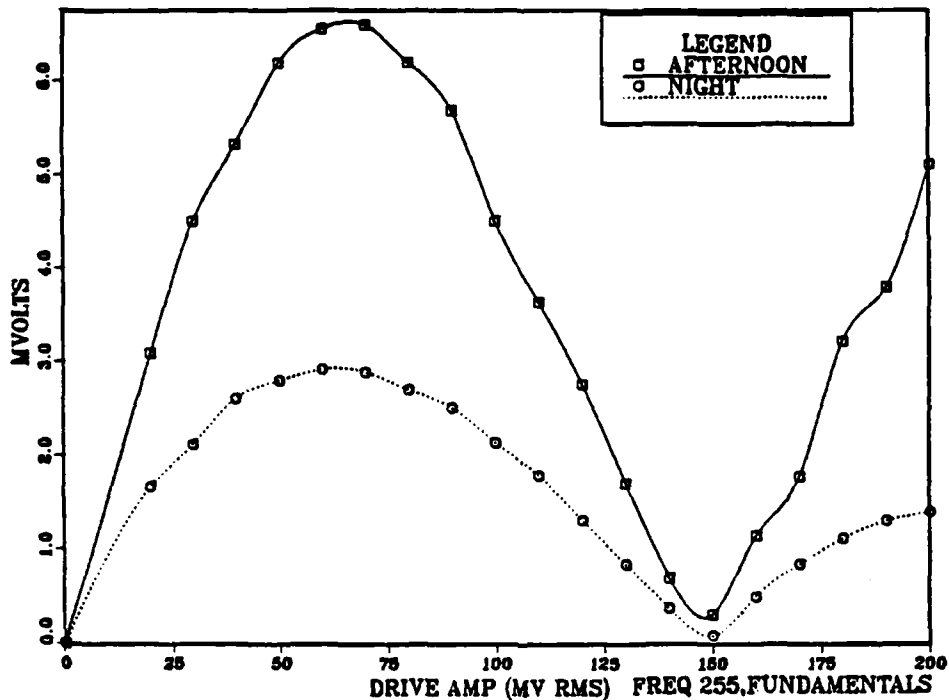


Figure 2.6 Polarization Drift.

where the dot products account for the different polarizations, x is the amplitude of waveguide length optical variations, and J_n is a Bessel function of order n . The modulation depth or fringe visibility is determined by the ratio of the static terms to the time varying terms above. Substituting the phase modulation, $\Delta\psi$ for kx , the photodetector response (current, $i(t)$) to this intensity modulated optical wave is given by:

$$\begin{aligned}
 i(t) = & i_0 \cos\psi_0 \left[J_0(\Delta\psi) \right. \\
 & + 2 \sum_{n=1}^{\infty} J_{2n}(\Delta\psi) \cos(2n(\omega_a t)) \left. \right] \quad (\text{eqn 2.16}) \\
 & - i_0 \sin\psi_0 \left[2 \sum_{m=0}^{\infty} J_{2m+1}(\Delta\psi) \sin((2m+1) \omega_a t) \right]
 \end{aligned}$$

This final expression reveals that the sensor's low frequency output current is a series of weighted harmonics of the sensed acoustic frequency. The weighting factor for

each term is a function of the acoustic pressure (via the $\Delta\psi$ parameter) that varies as the Bessel function of corresponding order. The relative magnitude of the Bessel functions are dependent on ψ_0 , a non-acoustic phase difference. A plot of maximum photodetector response as a function of acoustically induced phase shift is presented in Figure 2.7 [Ref. 13: p. 87]. Most current interferometric type sensors operate on the approximately linear region of the curve for the fundamental, that is the J_1 term in equation 2.16 for simplicity, thereby necessitating an upper limit on acoustically induced phase shifts of approximately one radian. [Ref. 8: pp. 12-13]

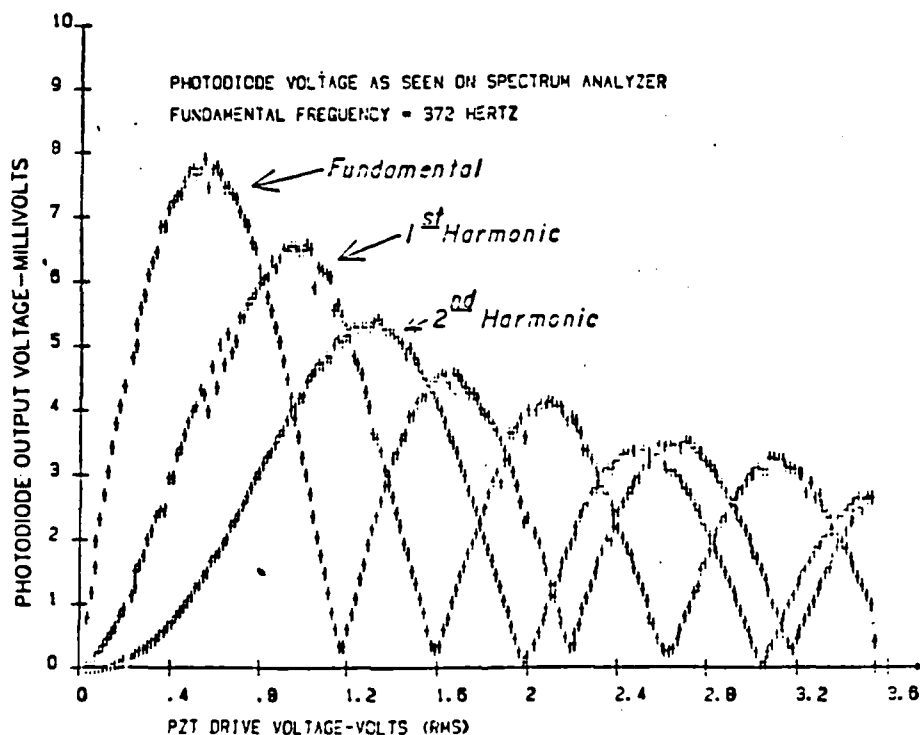


Figure 2.7 Photodiode Bessel Function Response.

It is noted that not only does the sensing electric field vector change relative to the reference electric field vector because of twisting and birefringence (modulation depth), but that the sum of these two vectors, $E_p(t)$,

changes with acoustic pressure, temperature, etc. (modulation rate). Note that for a given acoustic phase modulation $\Delta\psi \ll \pi$ the maximum photodetector response occurs when $\psi_0 = \pi/2$ as shown in Figure 2.8a. When $\psi_0 = \pi$ or 0 as shown in Figure 2.8b, the same acoustic modulation, $\Delta\psi$, leads to a photodetector current modulation of smaller amplitude at twice the acoustic frequency. For large acoustic phase modulation, $\Delta\psi \gg \pi$, as shown in Figure 2.8c, the photodetector current can have several frequency components which are harmonically related to the acoustic frequency. This explains the results shown in Figure 2.7. Needless to say, with polarization effects and acoustic and non-acoustic phase differences all occurring at the same time, demodulation is not easy.

2. Michelson Interferometer

An all-fiber Michelson interferometer is shown in Figure 2.9. The coherent light from the laser is split by the 3-dB coupler sending 50 percent of the light down each of the two sensor arms. Due to the nature of single mode transmission, the light hits the boundary surface (cleaved end) at $\theta = 0^\circ$. As stated in [Ref. 17], the incident plane becomes undefined and any distinction between the parallel and perpendicular components of reflectance and transmittance vanish so that:

$$R = \left[\frac{(n_{\text{core}} - n_{\text{cladding}})}{(n_{\text{core}} + n_{\text{cladding}})} \right]^2 \quad (\text{eqn 2.17})$$

For the Michelson interferometers built, this would suggest a 3.5 percent (-29 dB) reflectance of the lightwave back down the fiber. At the 3-dB coupler, the light is recombined with 50 percent of the light of sensor arm 1 and 50 percent of the light of sensor arm 2 returning to the laser and going to the photodetector. This path provides the light with two times the acoustic interaction length as

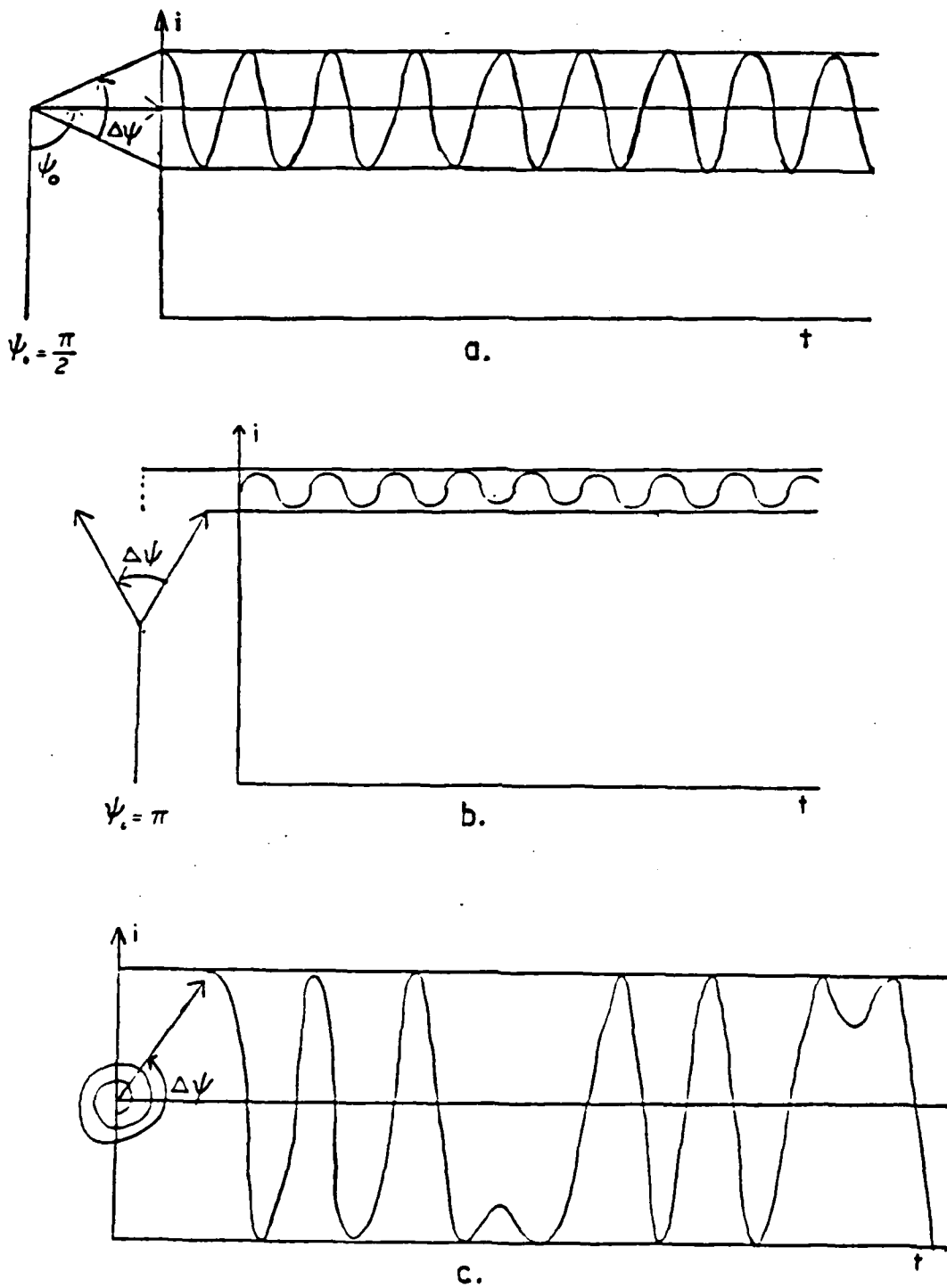


Figure 2.8 Electric Field Vector Summary.

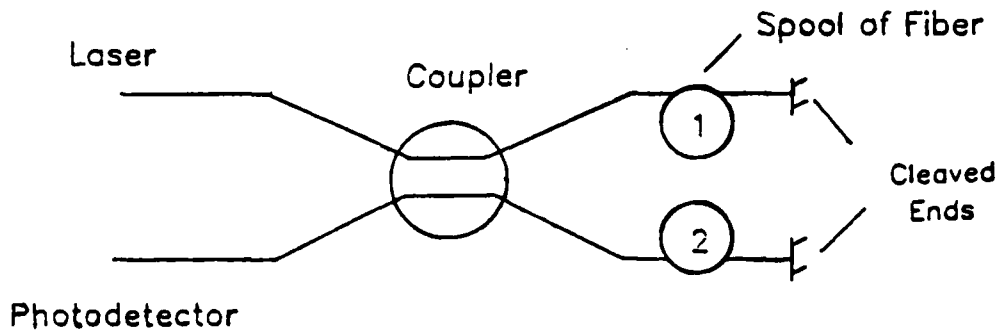


Figure 2.9 All-Fiber Michelson Interferometer.

compared with a Mach-Zehnder interferometer. This occurs because the light traverses the distance affected by pressure twice. Therefore, the phase accumulation will be doubled and the Michelson interferometer should be twice as sensitive as a Mach-Zehnder with the same sensing coil length.

REPRODUCED AT GOVERNMENT EXPENSE

III. EXPERIMENTAL APPARATUS

A. MICHELSON INTERFEROMETER DESIGN AND CONSTRUCTION

As shown in Figure 3.1, an optical fiber Michelson interferometer consists of a laser source, 3-dB coupler, fiber, and a photodetector. A brief description of the overall system will be presented with a detailed description of each individual part to follow.

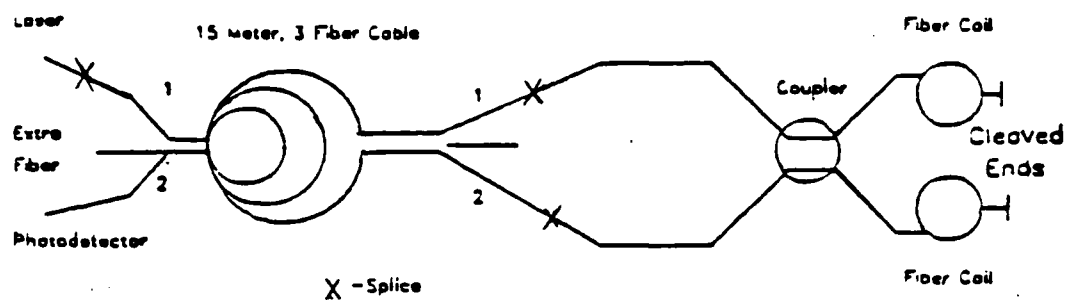


Figure 3.1 Optical Fiber Michelson Interferometer.

All of the fiber used in the interferometer was of the same particular single mode type manufactured by Corning. The 3-dB coupler was assembled by Aster, Inc. with ten meter long output leads on one side and two meter leads on the other side. With reference to Figure 3.1, the coherent laser source, pigtailed with the same type of Corning fiber, was spliced to one end, (1), of the 15 meter, three fiber cable with the other end of (1) spliced to one of the two meter coupler leads. Since the two fibers that were spliced were of the same type, fusing was not difficult. The two ten meter leads were wrapped around individual Teflon mandrels. Another fiber in the three fiber cable (2) was

spliced to the remaining two meter input lead. At the other end of (2), a photodetector was attached.

Coherent light from the laser is split at the 3-dB coupler and sent to the two fiber coils. The light travels to the partially reflecting ends and is reflected back toward the coupler. The light is recombined in the coupler and half of it goes to the photodetector and half to the laser. The interferometer converts phase modulation to intensity modulation which occurs when the recombined light interferes.

B. INTERFEROMETER COMPONENTS

1. Fiber

The optical fiber used for the two sensors was developmental optical fiber from Corning. It had a cladding outer diameter of 75 microns and the coating was UV cured acrylate. The fiber had a 3.2 dB/km loss.

2. Laser Source

The laser used for both systems was manufactured by M/A-COM Laser Diode Inc., specifically a LDT-358 from lot number C-146 #11. The device produced a coherent light of wavelength 847.1 nm. The laser power vs source current is shown in Figure 3.2. The extrapolated threshold current is 38.2 milliamps. The laser current was maintained at 42.0 milliamps in the experiments described herein. Power for the laser was provided by a 12 volt, 18 amp-hr, gel cell battery through a current regulating circuit. This circuit provided a constant current to the laser as described by Mills, [Ref. 13: pp.44-47].

3. Polarization Controller

A polarization controller, mounted at the output (pigtail) of the laser, as described by Lefevre [Ref. 18] was used in this experiment. It consists of two circular disks around which the fiber is wound. By bending the fiber around the small disks, stress birefringence was induced.

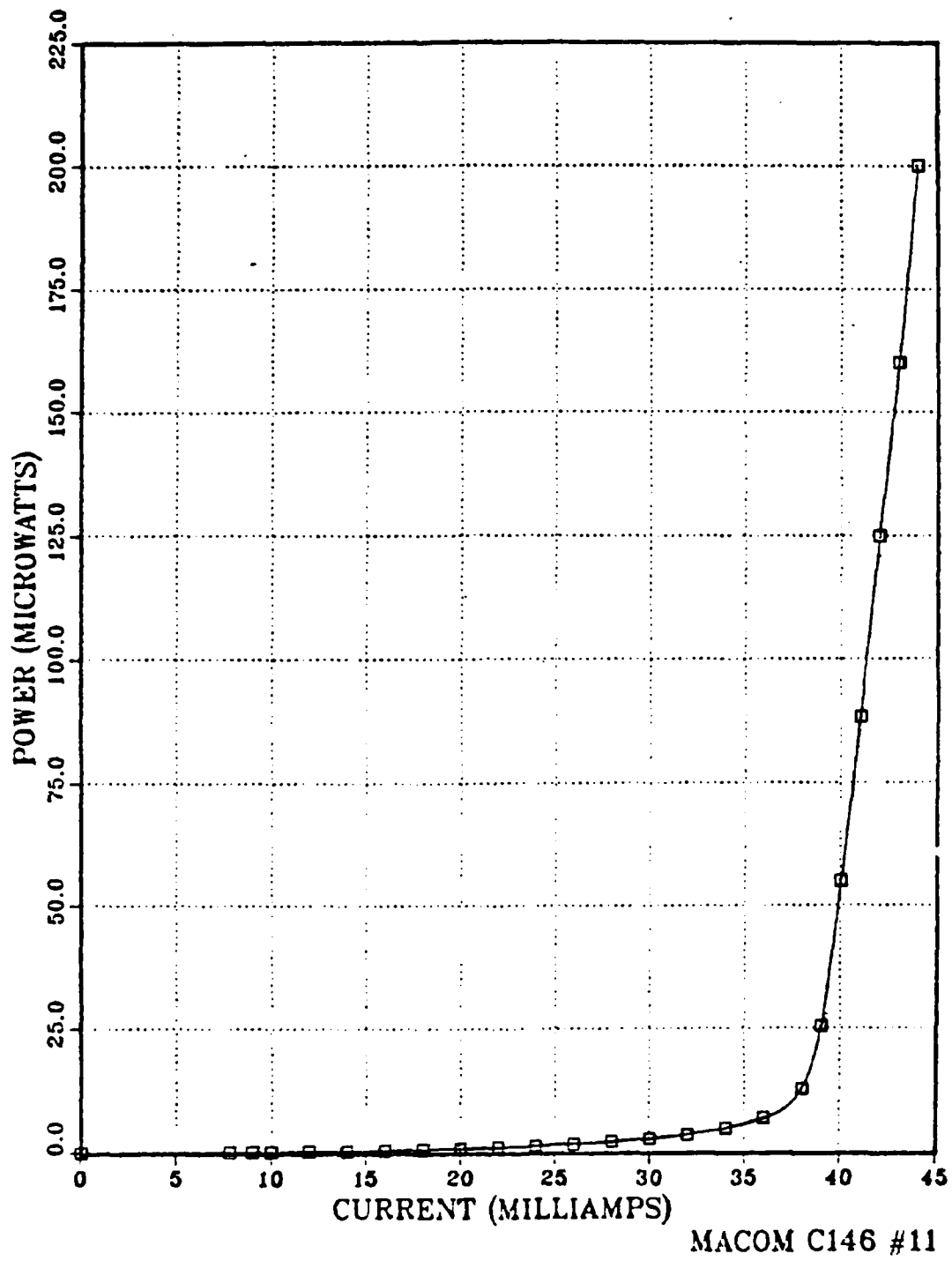


Figure 3.2 Laser Power vs. Source Current.

Using this device it was possible to adjust the polarization of the light entering the interferometer thereby allowing optimization of the fringe visibility. This device is equivalent to quarter wave plates of classical optics.

4. 3-dB Coupler

The 2x2 single mode couplers were made to specifications by Aster, Inc. with two meter input leads and 10 meter output or sensing coil leads, thus allowing assembly of the entire sensor and cable with only three splices. It is possible to have only one splice (from the laser pigtail on to one of the two meter leads) but the 15 meter, three fiber cable was added to allow for tank testing.

5. Cable

The "B" series fiberoptic cable was manufactured by Optical Cable Corporation and had an outer diameter of 0.7 cm. Besides three fibers, two strength members and reinforcing kevlar are used in the cable. The fibers had an additional loose fitting plastic jacket covered by an outer polyethelene case.

6. Teflon Mandrels

The 10 meter long output leads from the 3-dB coupler were wound around two Teflon mandrels. Each mandrel has an outer diameter of 4.1 cm and the bulk modulus of Teflon (polytetrafluoroethylene) is 2.78×10^9 Pa according to Hughes and Jarzynski [Ref. 19].

7. Partially Reflecting Ends

The partially reflecting ends of the fiber quite simply are cleaved ends encased in a plastic "bubble" which was fabricated from a short length (~ 1 cm) of Teflon "spaghetti" (1.0 mm O.D.). In order for the light to reflect, a large difference in the index of refraction is needed. Leaving the ends exposed, the index mismatch between the fiber and water would be quite small. Keeping the ends in air provides a sufficient index of refraction

mismatch to reflect the needed light. Figure 3.3 is a schematic of a bubbled end.

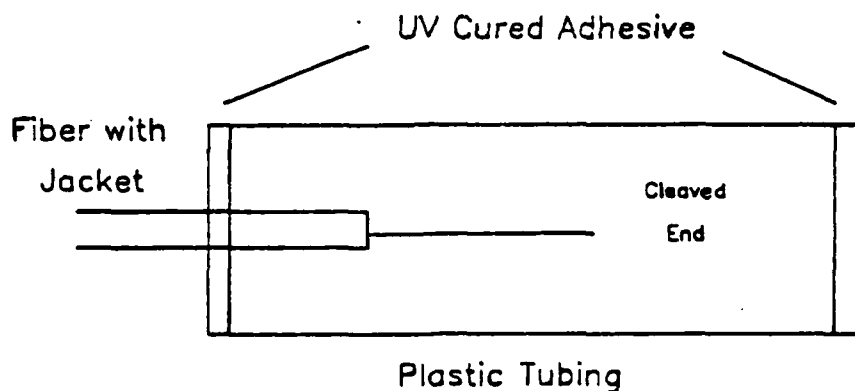


Figure 3.3 Cleaved End of a Ten Meter Lead.

8. Power Meter

The power meter used to detect the optical output of the fiber during construction of the sensors was a Coherent Model 212. It has full scale ranges of 0.1 microwatts to 10 milliwatts. The power meter provided an analog measure of the modulation depth (fringe visibility) of the signal during construction. However, the meter had a poor high frequency response and could not be used for data acquisition at acoustic frequencies.

9. Photodetector

The photodetector used for acoustic data acquisition was a Clairex type CLD-41. It is an all silicon PN planar diode with fast response, high linearity and low dark current. The electrical specifications are:

Active Area:	1.3 x 1.3 millimeters
Short Circuit Current:	min 6 to max 12 microamps
Open Circuit Voltage:	0.40 volts typical
Dark Current:	1 nanoamp
Junction Capacitance:	200 picofarads
Rise or Fall Time:	5 microseconds
Temperature Coefficient:	+.2%/degree typical
Peak Spectral Response:	0.91 micrometers

C. CONSTRUCTION OF MICHELSON INTERFEROMETER

Initially the laser and one of the two meter input leads of the coupler were spliced to opposite ends of one of the fibers in the 15m cable. The remaining two meter input lead was cleaved and attached to the photodetector so the system could be monitored during winding. The "T-bar" shown in Figure 3.4 was built to house the coupler and to hold the mandrels. The coupler was laid in place and secured with window caulking.⁴ Long plastic tubing was put around the fiber as it came out of the coupler. This was to protect the delicate fiber as it transitioned from the shaft to the mandrels. Referring to Figure 3.4, an extra piece of Teflon was added to guide the fiber from the shaft to the mandrel. Next, the two 10 meter fibers were cleaved and measured.

When building the first system, the modulation depth was quite large (>50%) from the beginning of construction. The fiber lengths only differed by 1.23 cm. When the second system was begun, the modulation depth was small (<3%). However, upon measurement of the fiber lengths, it was noted that they differed by 10.5 cm. Upon cutting them to within 0.95 cm, the modulation depth again rose to above 50%. This effect is due to the short spatial coherence length of the diode laser.

The bubble covers for the partially reflecting ends were placed on the fibers and held in place with ultraviolet (UV) curing glue.⁵ The fibers were wound onto temporary mandrels beginning at the bubbled end and winding up to the T-bar. The temporary mandrel was then set into a device that allowed for precision winding onto the permanent mandrels. Each layer consisted of approximately 83 turns with about 2 1/4 layers needed for the 10 meters of fiber. Each layer

⁴Frost King Fingertip Caulk, Thermwell Products Co., Inc.

⁵UV Curing Optical Adhesive, Norland Products, Inc.

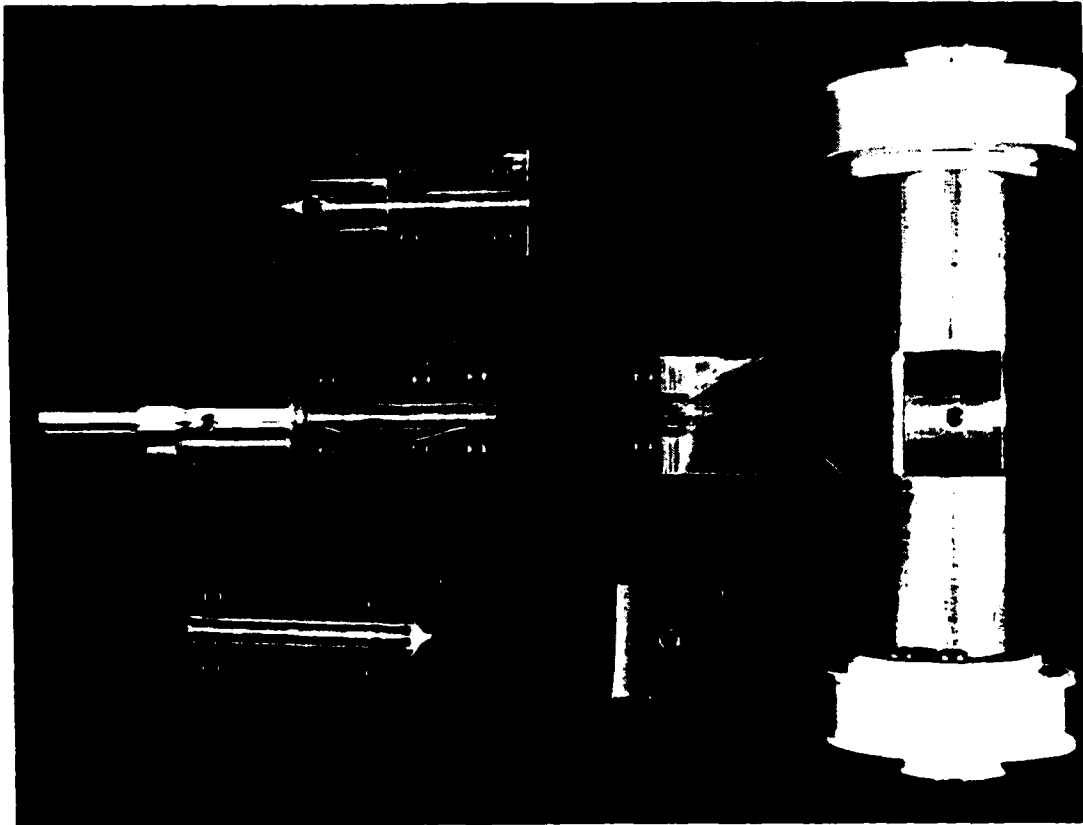


Figure 3.4. T-bar opened to reveal coupler.

was glued in place with a small amount of UV curing glue. When the bubbled end was on the Teflon mandrel, it was also glued into place. As the winding progressed, the modulation depth decreased as did the light output. However, checking the system the next day, the light output was still down some but not as much as immediately after winding. The modulation depth had returned to over 50%; as if the fibers had "relaxed" from the twisting of construction. After the UV glue had cured, the hydrophone was dipped in Plasti-Dip⁶ to protect the fibers.

⁶Plasti-Dip is a registered trademark of a product normally used to insulate the handles of small hand tools, pliers, etc.

The second system was built in the same manner with the exception of the winding procedure. The second T-bar was inadvertently built without the capability of holding the winding mechanism. For this reason, the fibers were wound by hand directly onto the Teflon mandrels. This second hydrophone was not dipped in Plasti-Dip.

D. INSTRUMENTATION

1. Signal Generation

In an earlier study [Ref. 14: pp.28-29], an acoustic calibrator was designed to test a gradient hydrophone with sensor coils ten centimeters apart. The same calibrator was used in this experiment. The calibrator was operated at two resonant frequencies, 255 Hz and 558 Hz. At each resonance, the spacing of the various pressure maxima and minima were measured and used to compute the sound speed in the calibrator for each frequency directly from the product of the measured frequency and wavelength. Table III provides the sound speeds at specific frequencies with a water depth of 39.2 cm in the calibrator.

TABLE III
SPEED OF SOUND IN 'SLOW WAVE' CALIBRATOR

Frequency(Hz)	Speed of Sound(m/sec)
255	289
558	250

The standing wave pressure field within the calibrator was examined using a standard LC-10 hydrophone. Figure 3.5 shows the standing wave acoustic field at the two resonant frequencies and a non-resonant frequency of 125 Hz.

A rotation mechanism using a potentiometer encoder was used to rotate the mandrel pair about a horizontal axis. The potentiometer provided a 0 ohm (0°) to 10,000 ohm (360°)

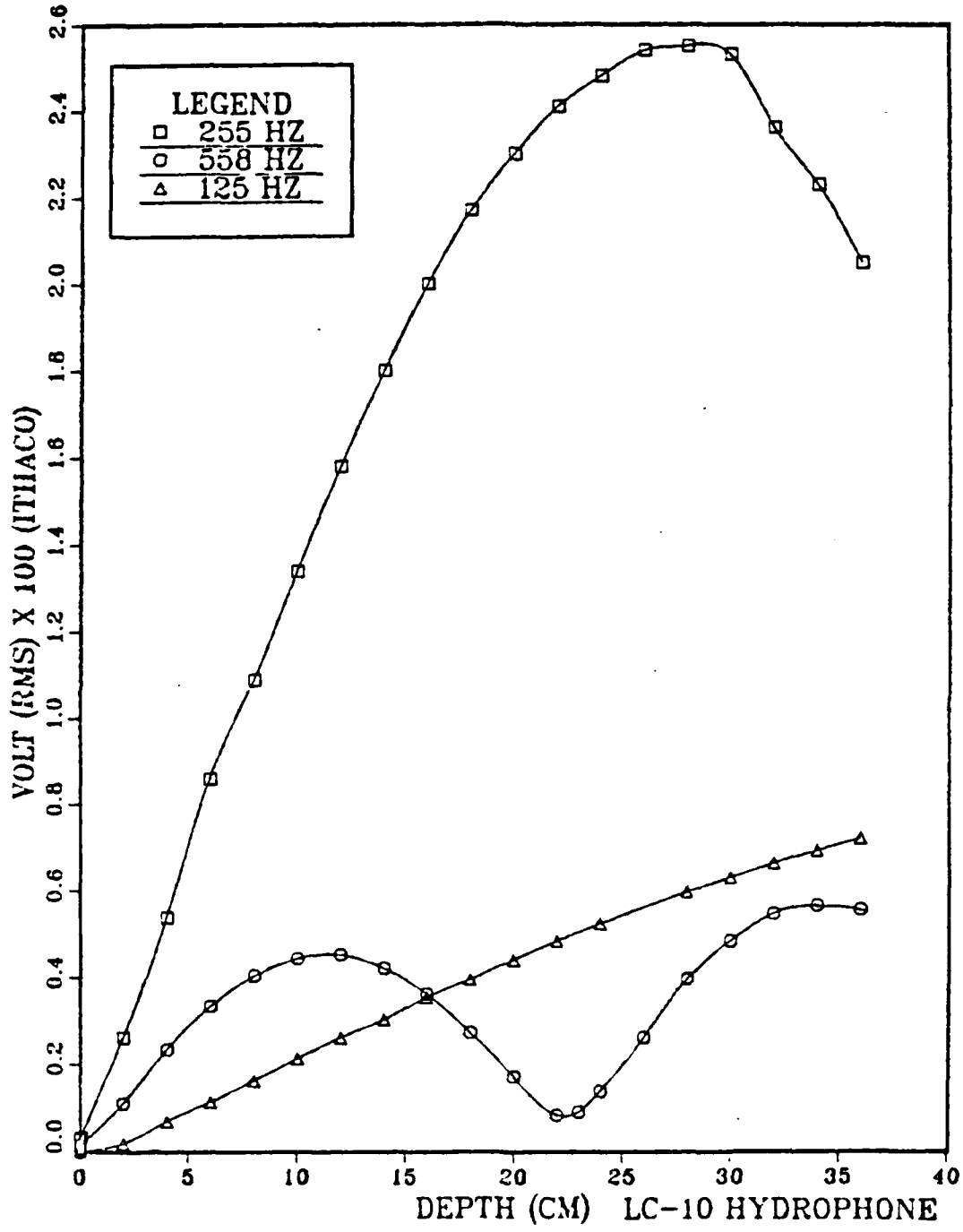


Figure 3.5 Standing Wave Acoustic Field vs. Depth.

angular readout which varied linearly with angular position. A Hewlett-Packard model 3478A digital multimeter was used to monitor the potentiometer and the hydrophone orientation. The calibrator tube was mounted on the face of a USRD J-11 acoustic projector [Ref. 20]. The projector's operating range is from 20 Hertz to 12 kHz with the maximum power above 100 Hz being 200 watts. A sinusoidal voltage was produced by a Hewlett-Packard model 3325 synthesizer/function generator and amplified by a Kikusui model POW35-1A bipolar power amplifier to drive the J-11 projector. The synthesizer/function generator has a frequency range from 1 μ Hertz to 21 MHzertz for a sine waveform and an output amplitude from 0 mvolts to 10 volts peak-to-peak. The amplifier can supply power from -35 volts to +35 volts continuously at 1 amp. It acts as an impedance match between the synthesizer/function generator and the J-11 and its gain was adjusted so the LED amplitude read-out of the HP 3325A would correspond to the rms voltage applied to the J-11. Figure 3.6 shows the electronic block diagram.

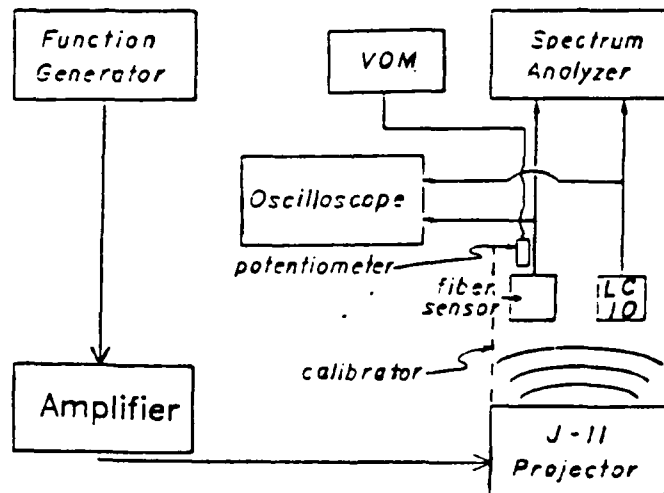


Figure 3.6 Electronic Block Diagram.

2. Detection

Detection of the optical signal depended upon zeroing the Bessel function, J_1 , as discussed in Chapter 2(C). An LC-10 hydrophone, serial number C-261, manufactured by Celesco, Inc., was used as the standard hydrophone for sensitivity determination of the fiber optic systems. The average low frequency free field sensitivity was given by the manufacturer to be -205.8 dB re 1 volt/micropascal. A Kikisui model COS-5060 oscilloscope was used to monitor the signal from the LC-10 hydrophone and the photodetector output of the optical fiber hydrophones. It is a dual channel 60 megaHz instrument with a calibrated vertical deflection from 1 mvolts to 5 volts per division and a horizontal calibrated sweep of 50 nsec to 0.5 seconds per division. The Hewlett-Packard model 3582A spectrum analyzer has a CRT which can display the rms amplitude of the fundamental and harmonic frequencies generated by the interferometer. By varying the amplitude of the synthesizer/function generator it is possible to visually determine the acoustic amplitude necessary to reduce to zero the photodetector output at the frequency of the acoustic signal i.e., to generate a phase shift of 3.83 radians which zeroes the J_1 Bessel function amplitude in equation 2.16

IV. EXPERIMENTAL PROCEDURE AND ANALYSIS

The first system built, the dipped hydrophone, was tested to confirm proper interferometric properties. The second system, the undipped hydrophone, was built and tested upon completion of all testing of the dipped hydrophone. Thus, the order of experiments and techniques used on the second hydrophone benefitted from the knowledge gained from building the first hydrophone. The results for both hydrophones are given below.

A. DIPPED HYDROPHONE

The gradient sensor, with coils spaced 10 cm apart, was placed in the acoustic calibrator at specific depths for specific frequencies.

1. Experimental Procedure at 255 Hz

Referring to Figure 3.5, the extended region of constant gradient at 255 Hz provided an excellent region in which to place the hydrophone. With an approximate constant gradient from 3 cm to 17 cm, the 10 cm hydrophone was easily accommodated. The sensor axis and LC-10 acoustic center were placed at a depth of 10 cm. Setting the synthesizer frequency to 255 Hz, the drive voltage to the acoustic calibrator was increased until the fundamental frequency reached its minimum value. This was determined by visually monitoring the HP-3582A spectrum analyser. The voltage of the LC-10, V_{LC-10} , and the J-11 drive voltage, V_{J-11} , were recorded. The sensor was rotated 10° and the procedure was repeated until the hydrophone had made a 360° rotation. Referring to the discussion of the Bessel function in Chapter 2(C), the sensitivity of the gradient hydrophone could be calculated. The first zero value of the Bessel function J_1 occurs at 3.83 radians. Again referring to

Figure 3.5, at 255 Hz and 1 volt RMS drive, the LC-10 voltage at the pressure maximum was .023 volts. The J-11 drive voltage/Pa could then be calculated using:

$$V_{J-11}/Pa = \frac{((1v \text{ rms J-11 drive}) * M_{LC-10}(v/Pa))}{\text{max LC-10}(v)} \quad (\text{eqn 4.1})$$

where M_{LC-10} is the sensitivity of the LC-10 hydrophone. This datum was obtained from the manufacturer.

The units of acousto-optical sensitivity, M_{optic} , are in rad/Pa. In this case the $V_{J-11}/Pa = 2.00 \text{ mv/Pa}$. The sensitivity of the fiber optic hydrophone was calculated using:

$$M_{\text{optic}} = (3.83 \text{ (rad)} * 2.00(\text{mv/Pa})) / V_{J-11}(\text{mv}) \quad (\text{eqn 4.2})$$

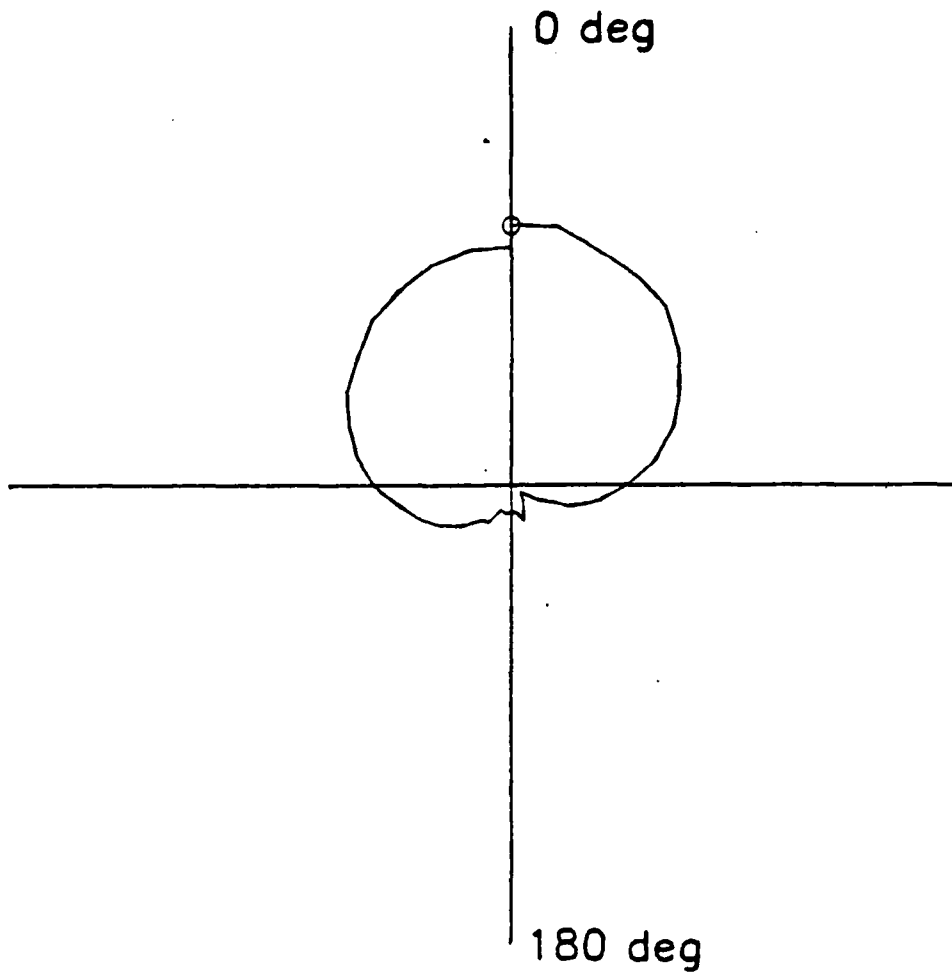
Figure 4.1 shows the directional sensitivity of the dipped hydrophone with the angle of maximum sensitivity marked.

2. Experimental Procedure at 558 Hz

Referring again to figure 3.5, at 558 Hz, there is not a large enough region of constant gradient to accommodate the 10 cm hydrophone. Hence, the sensor was placed at the standing wave pressure minimum, 22.5 cm. This placed each individual sensor in a region of maximum pressure gradient. The data was taken in the same manner as in the 255 Hz test. Again referring to Figure 3.5, at 558 Hz and 1 volt RMS drive, the LC-10 voltage at the pressure maximum is 4.58×10^{-3} volts. In this case the $V_{J-11}/Pa = 11.2 \text{ mv/Pa}$. The J-11 voltage was recorded at the fundamental minimum and the sensitivity was then calculated using equation 4.2. Figure 4.2 shows the resulting sensitivities.

3. Single Coil and Temperature Sensitivities

The sensitivities at 255 Hz and 558 Hz for the dipped gradient hydrophone shown in Figures 4.1 and 4.2 were



MAXIMUM SENSITIVITY = .085 rad/Pa

Figure 4.1 Directional Sensitivity of Dipped Hydrophone
at 255 Hz.

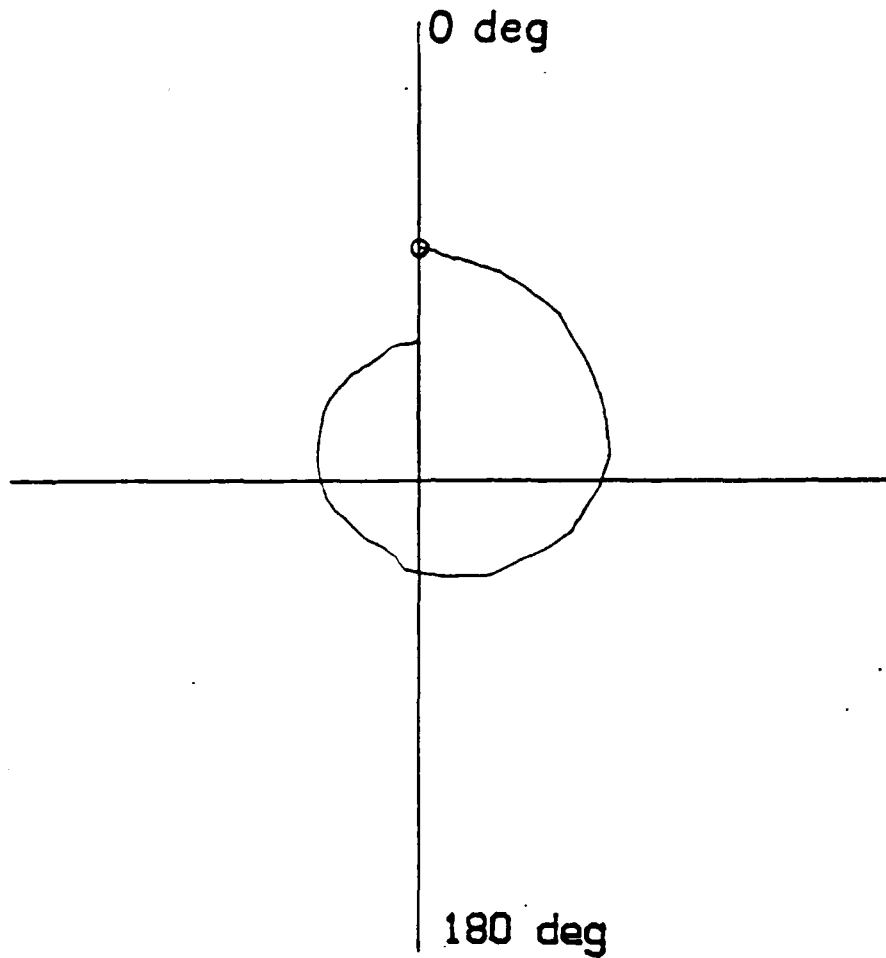
not as expected. Single coil and temperature sensitivity tests were done to provide additional information about the sensor to resolve this mystery.

The sensitivity of each individual coil was determined by placing a single coil in the calibrator with the other coil remaining just above the water-air interface. As depicted in Figure 4.3, this places the submerged coil at a depth of approximately 7 cm. The acoustic center of the reference LC-10 hydrophone was placed at 7 cm as well. As in the 255 Hz case, the fundamental Bessel function was driven to a minimum, the LC-10 voltage recorded, and the sensitivity calculated. The hydrophone was then turned 180° and the other coil's sensitivity was measured.

The water in the calibrator was then cooled 7.2° C and the single coil sensitivities measured. Table IV provides the results of the two tests. The system is very temperature dependent.

These results explain the two directional sensitivity plots in Figures 4.1 and 4.2. Referring to Chapter 2(A,2), in a standing wave field, an unbalanced hydrophone will produce a directional sensitivity pattern of a cardioid at a specific frequency. For a ratio of 2.82, Figure 4.4 depicts the theoretical patterns at 255 Hz and 558 Hz.

The non-closures of the two outputs can be explained by the temperature dependence. Each 360° run takes approximately 2-3 hours to complete. With MacDonald [Ref. 14], this same setup was computer controlled and took approximately 15 minutes for each run. The difference is due to the stability of the new system. Approximately five minutes after the hydrophone is immersed in the calibrator tube, the non-acoustic portions of the electric field vectors stabilize and do not move relative to each other so that there is no variation of the static phase ψ_0 . If the static phase, ψ_0 , stagnates the photodetector current cannot achieve all



MAXIMUM SENSITIVITY = .383 rad/Pa

Figure 4.2 Directional Sensitivity of Dipped Hydrophone at 558 Hz.

REPRODUCED AT GOVERNMENT EXPENSE

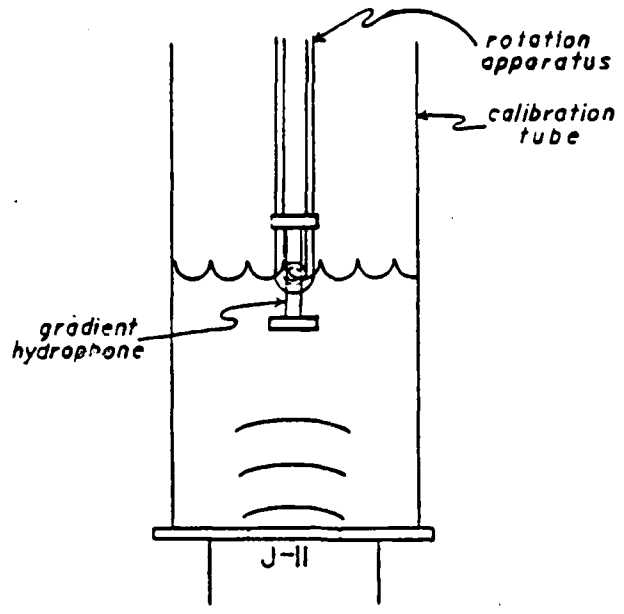


Figure 4.3 Single Coil Sensitivity Experimental Setup.

TABLE IV
SINGLE COIL AND TEMPERATURE SENSITIVITIES
OF DIPPED HYDROPHONES

Freq (Hz)	Temperature 17.2°C			Temperature 10.0° C		
	* Coil#1 (rad/Pa)	* Coil#2 (rad/Pa)	* Ratio	* Coil#1 (rad/Pa)	* Coil#2 (rad/Pa)	* Ratio
255	* .205	* .072	* 2.86	* 1.09	* .142	* 7.67
558	* .214	* .077	* 2.78	* .990	* .137	* 7.23

of the possible values available in equation 2.16, and accurate determination of the acoustic field necessary to drive the J_1 Bessel function to zero may not be obtainable.

A full sweep of the static phase factor, ψ_0 , given in equation 2.16 is needed to determine the acoustic amplitude which minimizes the fundamental J_1 Bessel function output. Physically touching the coils, stirring the water, or applying a heating device to the water were techniques used to keep the modulation rate moving. Using the heating device occasionally during the run increased the temperature

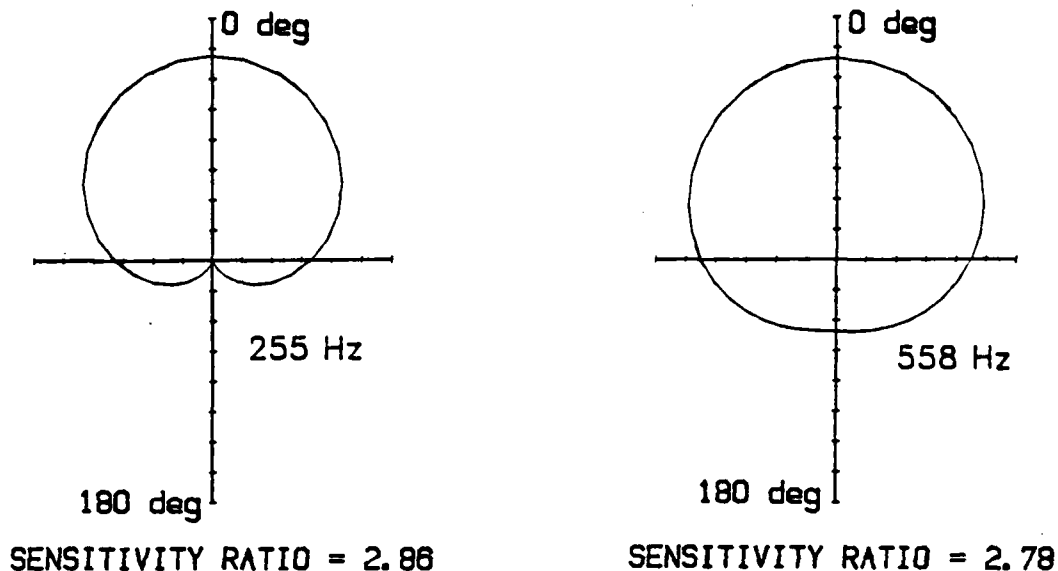


Figure 4.4 Theoretical Sensitivity Patterns of Dipped Hydrophone.

in the water and thus modified the sensitivity and sensitivity ratio of the hydrophone. This is particularly noticeable in the case of 558 Hz. With the sensor 22.5 cm below the surface, directing the heat at the surface did not have much effect as compared to the 10 cm depth at 255 Hz. Stirring the water to move any thermal gradients and reaching into the calibrator to grasp the sensor did not work well either. Therefore, at approximately 250° the heating device was turned on for 5-10 minutes to heat the outside of the calibrator at the depth of the sensor. This sharply increased the static phase modulation rate and the rest of the experimental run progressed smoothly and quickly. However, the increase in temperature decreased the sensitivity of the sensor and the consequence is quite noticeable.

B. UNDIPPED HYDROPHONE

The results of the temperature test suggested that the Plasti-Dipped rubber compound was having a pronounced effect

on the hydrophone. The second system was not dipped and the single coil and temperature sensitivities were measured first. The procedure used in these tests was the same as for the dipped hydrophone and Table V summarizes the results.

TABLE V
SINGLE COIL AND TEMPERATURE SENSITIVITIES
OF UNDIPPED HYDROPHONE

Freq (Hz)	Temperature 17.8°C			*	Temperature 12.3° C		
	* Coil#1 (rad/Pa)	Coil#2 (rad/Pa)	Ratio		* Coil#1 (rad/Pa)	Coil#2 (rad/Pa)	Ratio
125	* .705	.705	1.00	*			
258	* .705	.613	1.15	*	.718	.769	0.93
532	* .559	.545	1.03	*	.656	.683	0.96

The sensor was then placed at 10 cm (258Hz) and 22.5 cm (532 Hz) and the gradient hydrophone sensitivities were measured. All computations were done in the same format as the dipped hydrophone. An additional 125 Hz test was also included. The 125 Hz test had the hydrophone placed at 25 cm (see Figure 3.5). Figures 4.5, 4.6, and 4.7 provide the theoretical and measured directional sensitivities of the undipped gradient hydrophone at 125 Hz, 258 Hz, and 532 Hz respectively. The approximately 10% difference between the two coils accounts for one loop being larger than the other and the minimums at 90° and 270° not fully going to zero.

The non-closures for 258 Hz and 532 Hz is believed to be due to temperature sensitivities which are much weaker than the Plasi-Dip units. In the case of 532 Hz the laser's internal photodetector displayed 0.248 mamps at the beginning of the run and 0.241 mamps when the experiment was finished 2.25 hours later.

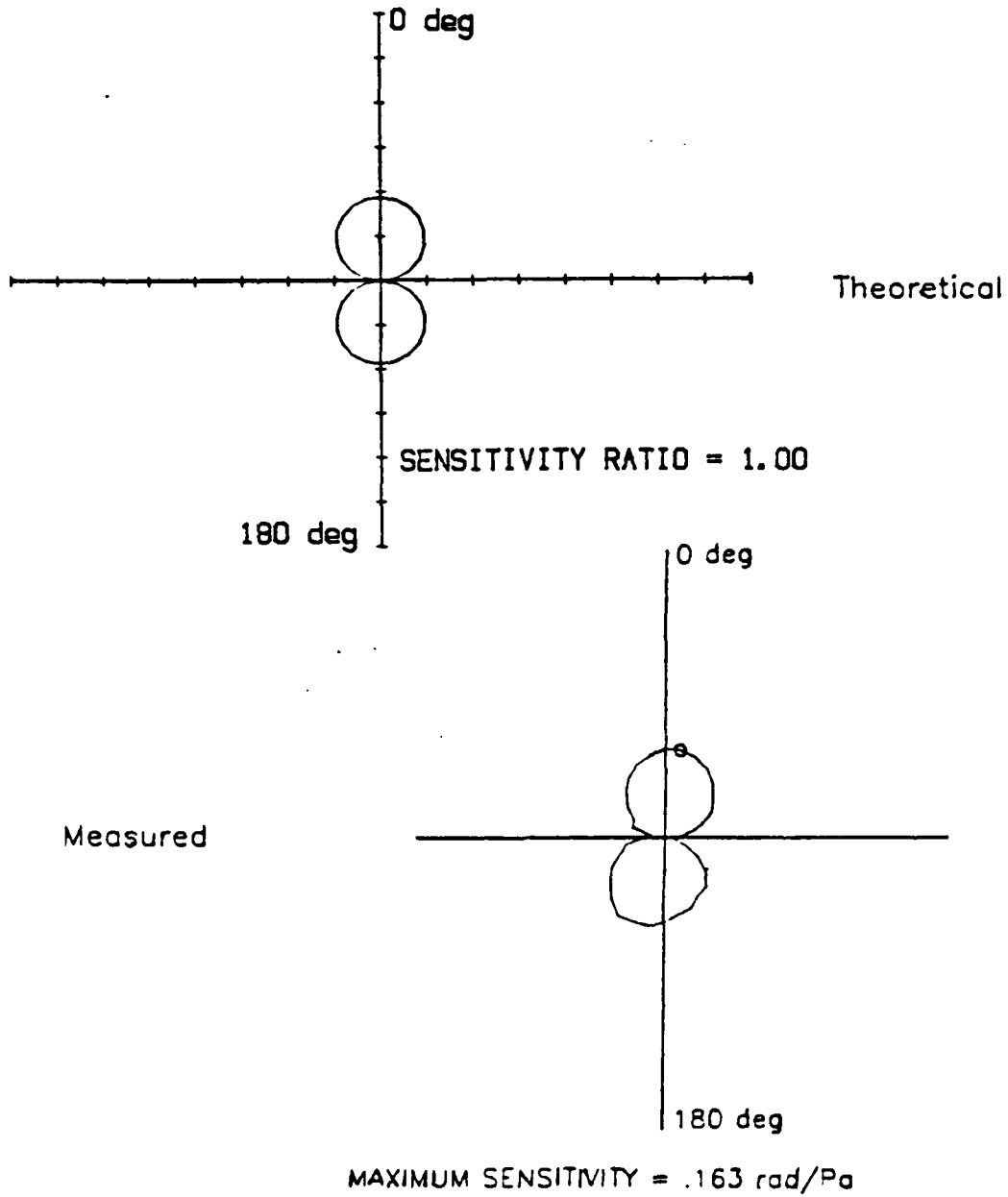


Figure 4.5 Theoretical and Measured Sensitivities of Undipped Hydrophone at 125 Hz.

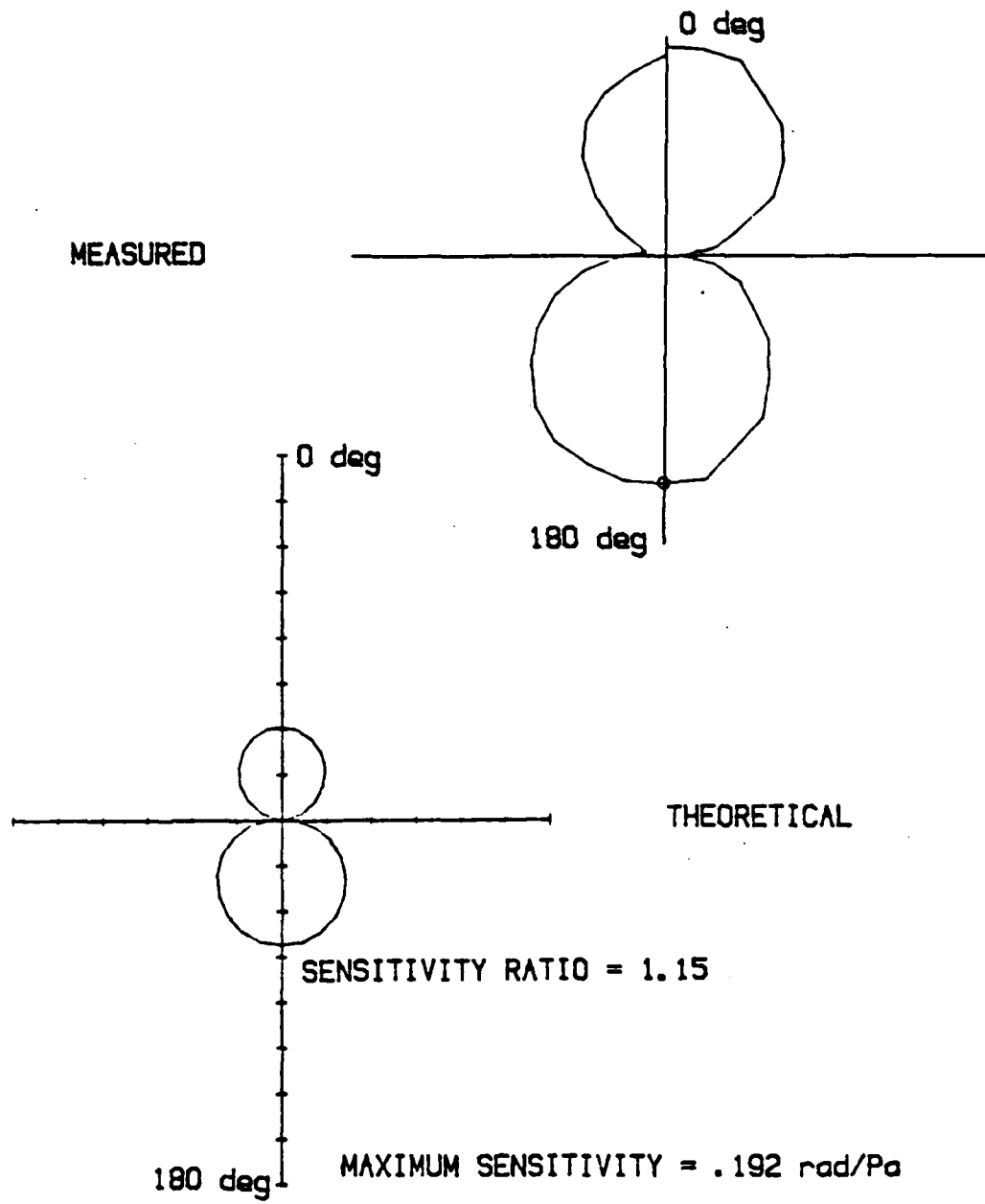


Figure 4.6 Theoretical and Measured Sensitivities of Undipped Hydrophone at 258 Hz.

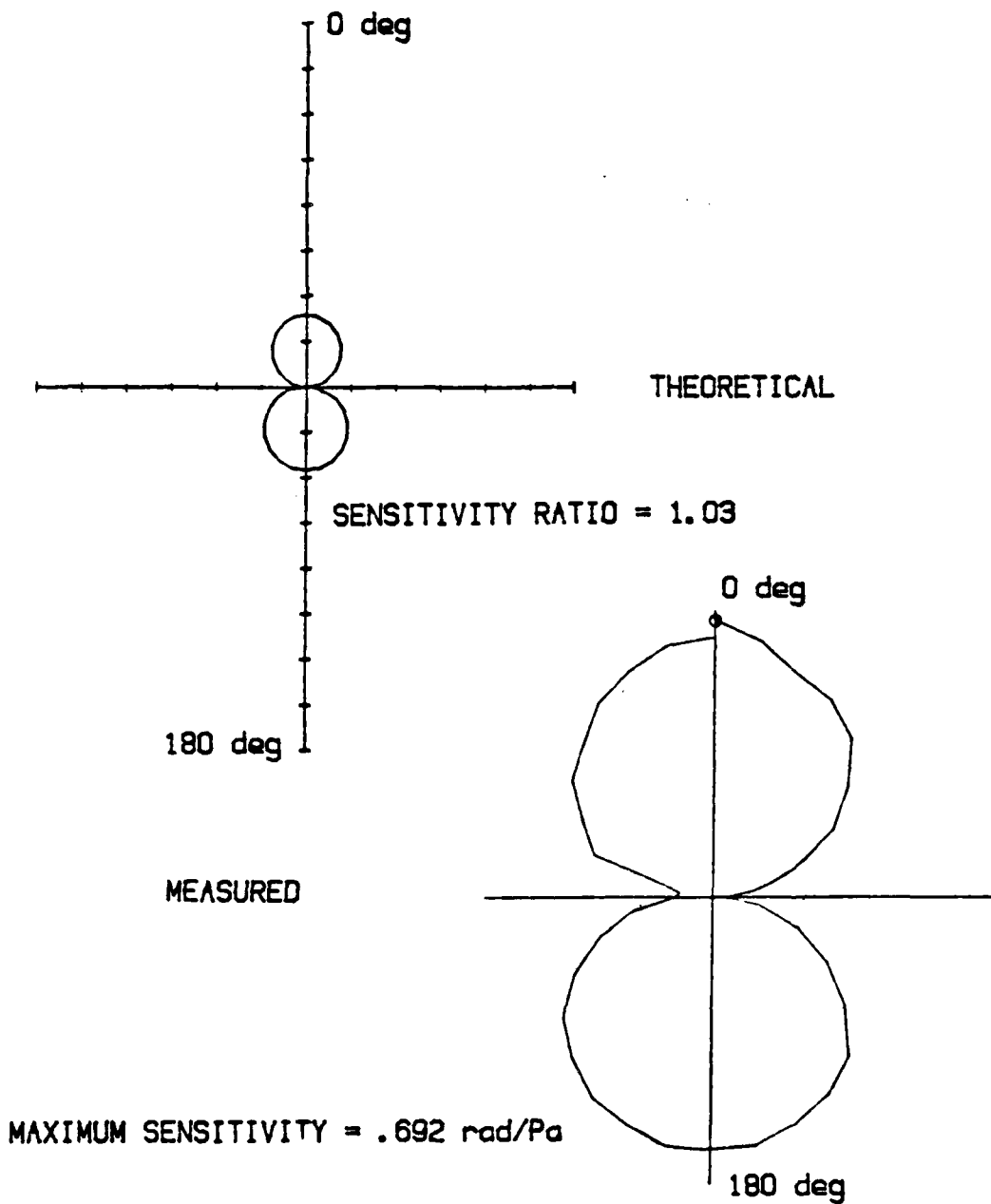


Figure 4.7 Theoretical and Measured Sensitivities of Undipped Hydrophone at 532 Hz.

V. CONCLUSIONS

A. SUMMARY OF RESULTS

Gradient sensor sensitivity can be calculated directly from the single coil sensitivity using equations 5.1 and 5.2.

$$\Delta\Phi = (M_1 + M_2)P_0Kd/2 \quad (\text{eqn 5.1})$$

$$M_{\text{gradient}} = \Delta\Phi/P_0 = (M_1 + M_2)\pi fd/c \quad (\text{eqn 5.2})$$

where P_0 is the pressure at the first maximum. Table VI compares the maximum gradient sensor sensitivities as calculated from the single coil sensitivities with those actually measured.

The results of Table VI show the single coil sensitivities to be relatively frequency independent with an average sensitivity of $.64 \pm .08$ rad/Pa. Except for 258 Hz, the gradient hydrophone sensitivities show proper frequency dependence, unlike the results of Cuomo [Ref. 21].

In order to compare the above results with those of MacDonald [Ref. 14], who used Stycast 1266 expoy mandrels, the material characteristics of the Teflon mandrels were analyzed. From the definition of the bulk modulus, $B = \Delta P/(\Delta V/V)$, we can imply equations 5.3 and 5.4.

$$\Delta V/V = \Delta P/B = 3\Delta L/L \quad (\text{eqn 5.3})$$

$$\Delta L/L\Delta P = 1/3B = (3B)^{-1} \quad (\text{eqn 5.4})$$

TABLE VI
GRADIENT SENSOR SENSITIVITIES

17.2 deg c			Theoretical Gradient rad/Pa	Measured Gradient rad/Pa	<u>Meas.</u> Grad.
Freq Hz	Coil #1 rad/Pa	Coil #2 rad/Pa			
125	.705	.705	.192	.163	.85
258	.613	.705	.370	.192	.52
532	.545	.559	.739	.692	.94

Using the value of $B = 2.78 \times 10^9$ Pa [Ref. 19] from equation 5.4, $\Delta L/L = 1.2 \times 10^{-10}$ m/Pa. For 20 meters of fiber, $\Delta L = 2.4 \times 10^{-9}$ m/Pa. For single mode fiber at a wavelength, $\lambda = 847.1$ nm, and a refractive index of 1.48, the wavelength of glass, λ_{glass} , is given by equation 5.5.

$$\begin{aligned} \lambda_{\text{glass}} &= (847.1 \times 10^{-9})/1.48 = 5.72 \times 10^{-7} \text{ m} \\ &= 5724 \text{ \AA} \end{aligned} \quad (\text{eqn 5.5})$$

Hence the sensitivity should be:

$$\begin{aligned} M_{\text{teflon}} &= \Delta\Phi/\Delta P = 2\pi\Delta L/\lambda_{\text{glass}} \\ &= 2.6 \times 10^{-2} \text{ rad/Pa} \end{aligned} \quad (\text{eqn 5.6})$$

Comparing the measured average sensitivity of the single coils (.64 rad/Pa) to M_{teflon} (.026 rad/Pa) using the bulk modulus = 2.78×10^9 Pa given by Hughes and Jarzynski

[Ref. 19], it is noted that the measured sensitivities are 25 greater than predicted. An explanation of this result has not yet been determined. In MacDonald [Ref. 14: pp. 90-94], the calculated theoretical sensitivity for the Mach-Zehnder configuration using Stycast 1266 mandrels with 10 meters of fiber was 10.1×10^{-3} rad/Pa and a sensitivity of $11.1 \pm .6 \times 10^{-3}$ rad/Pa was measured.

Using the demodulation technique in Mills, [Ref. 13: pp. 94-95], one can make a comparison to the USRD type G63 standard pressure gradient hydrophone. Referring to Figure 2.7, at the minimum of the fundamental, the sensitivity of the piezoelectric phase shifter is $(1.18 \text{ v}) / (3.83 \text{ rad}) = 308 \text{ mv/rad}$. Extrapolating to 100 Hz, the theoretical gradient sensitivity is calculated to be 0.132 Rad/Pa and $M (100 \text{ Hz}) = (.132 \text{ rad/Pa})(308 \text{ mv/rad}) = 41 \text{ mv/Pa}$. At 100 Hz, the USRD type G63 sensitivity is .28 mv/Pa [Ref. 20]. This would suggest a 43 dB sensitivity advantage. At this point, the demodulation sensitivity could be made almost any value, just as the gain of the internal pre-amplifier in the G63 could be changed, and the true comparison of the two hydrophones would have to include other considerations such as noise floor or total system compatibility factors such as supply power, output impedance, etc.

B. CONCLUSIONS

The Michelson configuration inherently allows for improvements in fiber hydrophone construction. Because this configuration uses only one coupler and between one and three splices, simplicity of fabrication and ruggedness are enhanced and the possibility of light loss due to mechanical error is greatly reduced. Additionally, through the use of partially reflecting ends, the Michelson configuration effectively doubles the fiber length thereby doubling the sensitivity over a Mach-Zehnder configuration.

In a standing wave field, at specific wavelengths and coil spacings, equal sensitivities in a gradient hydrophone will produce a directional figure-eight pattern. If the coils are slightly unbalanced, the pattern does not produce nulls and one sensitivity along one axis will be larger than the other. Large, unequal coil sensitivities can cause the sensitivity pattern to become a cardioid. This is not the case in a traveling wave field, the unbalanced hydrophone will become omni-directional and not cardioid.

C. RECOMMENDATIONS

The cause of the factor of 25 in measured sensitivity over theoretical calculations must be determined and actual sea trials be performed to test the system in a real world environment. A demodulation scheme is needed which will readily produce the desired output. Although drawbacks (such as imbalancing) exist, the Michelson fiber optic hydrophone is the optimum pressure gradient device. Directional hydrophone designs based on accelerometers and velocimeters in neutrally buoyant cases which will provide a better impedance match to the water should be pursued.

LIST OF REFERENCES

1. McHenry, J.R., Fiber Optic Design Application for a Shallow Water Torpedo Tracking Range, Master's Thesis, Naval Postgraduate School, Monterey, California, 1979.
2. Powers, J.P., An Introduction to Fiber Optical Communications, class notes, Naval Postgraduate School, 1983.
3. Keiser, G., Fiber Optical Communications, McGraw-Hill, 1983.
4. Kleekamp, C. and Metcalf, B., Designer's Guide to Fiber Optics - Part 1, Cahners Publishing Company, 1978.
5. Davis, C.M., Carome, E.F., Weik, M.H., Ezikiel, S., and Einzig, R.E., Fiberoptic Sensor Technology Handbook, Dynamic Systems, Inc., McLean, Virginia, 1982.
6. Senior, J.M., Optical Fiber Communications Principles and Practice, Prentice-Hall International, Inc., 1985.
7. Stein, K.J., and others, "Technical Survey: Fiber Optics" - Part 1 Promising Future Seen for Optical Fibers," Aviation Week and Space Technology, p. 45, 12 October 1981.
8. Self, Richard E., Fiber Optic Acoustic Sensors, (unpublished), Naval Postgraduate School, Monterey, California, December, 1985.
9. Busurin, V.I., Semenov, A.S., and Udalov, N.P., "Optical and Fiber-optic Sensors (review)", Sov. J. Quantum Electron, 15 (5) pp. 595-621, May 1985.
10. Lyamshev, L.M. and Smirnov, Y.Y., "Fiber-Optic Acoustic Sensors (review)", Sov. Phys. Acoust., 29 (3) pp. 169-180, May 1983.
11. Beyer, R.T., Non-Linear Acoustics, Department of the Navy, pp. 295-297, 1974.
12. Mills, G.B., Garrett, S.L., and Carome, E.F., "Fiber Optic Gradient Hydrophone", Proceedings Society Photo-Optical Engineers, vol. 478, pp. 98-103 (1984).

13. Mills, Gary B., Fiber Optic Gradient Hydrophone, Master's Thesis, Naval Postgraduate School, Monterey, California, 1984. DTIC Report Number AD-A143 975
14. MacDonald, Glenn E., Fiber Optic Gradient Hydrophone Construction and Calibration for Sea Trial, Master's Thesis, Naval Postgraduate School, Monterey, California, 1985. DTIC Report Number AD-A156 469
15. Bobber, R.J., Underwater Electroacoustic Measurements, Naval Research Laboratory, 1970.
16. Carome, E.F., and Satyshur, M.P., Acoustically Induced Phase and Intensity Modulation in Optical Fibers, John Carroll Univ., Dept. of Physics, Technical Report PH 78-2, 1978.
17. Hecht, Eugene and Zajac, Alfred, Optics, Addison - Wesley Publishing Company, 1979.
18. Lefevre, H.C., "Single - Mode Fiber Fractional Wave Devices and Polarization Controllers", Electronics Letters, v. 16, p. 778, 1980.
19. Hughes, R., and Jarzynski, J., "Static Pressure Sensitivity Amplification in Interferometric Fiber-Optic Hydrophones", Applied Optics, 19, 98 (1980).
20. Underwater Electroacoustic Standard Transducer Catalogue, Underwater Sound Reference Detachment, Naval Research Laboratory, 1982.
21. Cuomo, F.W., "Pressure and Pressure Gradient Fiber-Optic Lever Hydrophones", Journal Acoustical Society of America, 73 (5) pp.1848-1857, May 1983.

BIBLIOGRAPHY

Kinsler, L.E., Frey, A.P., Coppens, A.B., Sanders, J.V.,
Fundamentals of Acoustics, Wiley, New York, 1982.

Olson, H.F., Acoustical Engineering, D. Van Nostrand
Company, Inc., New York, 1957.

INITIAL DISTRIBUTION LIST

	No.	Copies
1. Defense Technical Information Center Cameron Station Alexandria, VA 22304-6145	2	
2. Library, code 0142 Naval Postgraduate School Monterey, CA 93943	2	
3. Prof. S.L. Garrett Department of Physics (code 61Gx) Naval Postgraduate School Monterey, CA 93943	6	
4. Prof. E.F. Carome Department of Physics (code 61Cm) Naval Postgraduate School Monterey, CA 93943	3	
5. Commanding Officer Underwater Sound Reference Detachment Naval Research Laboratory ATTN: Dr. R.W. Timme (code 5970) P.O. Box 8337 Orlando, FL 32856	1	
6. R.E. Self, LT, USN BOQ Naval Sub Base-New London Box 18/Room 325 Groton, CT 06349	1	
7. C.L. Burmaster, LCDR, USN Physics Department (code 9c) United States Naval Academy Annapolis, MD 21402	1	
8. Dr. G.S.K. Wong Physics Division National Research Council Ottawa, CANADA K1A OSI	1	
9. Commanding Officer ATTN: LCDR M.B. Johnson Naval Underwater Systems Center Newport, RI 02481	1	
10. Commanding Officer Naval Ocean System Center Fiber Optic Technology ATTN: Mr. M. Brininstool (code 946) Mr. A. Estabrook (code 946) Mr. J. Ehlers (code 714) Lt. P.A. Feldmann (code 714) San Diego, CA 92152-5000	1 1 1 1	
11. Dr. Clark Penrod Applied Research Lab Environmental Acoustics Division University of Texas Austin, TX 78713-8029	1	

- 12. Dr. James West 1
 Acoustics Research Department
 AT&T Bell Laboratories
 600 Mountain View Ave.
 Murray Hill, NJ 07974

- 13. Space and Naval Warfare Systems Command
 Project ARIADNE PDW124-70
 ATTN: Capt. Kirk Evans 1
 Dr. G. Hetland 1
 Ron Mitnick 1
 Lt. B.R. Ogg 1
 Washington, D.C. 20363-5100

- 14. Lt. Peggy A. Feldmann 1
 P.O. Box 2102
 Monterey, CA 93942

- 15. Dr. E.E. Feldmann 1
 3918 Midvale Dr.
 San Antonio, TX 78229

END

DTIC

6-86